Turbulent oscillatory boundary layers at high Reynolds numbers

By B. L. JENSEN, B. M. SUMER AND J. FREDSØE

Technical University of Denmark, Institute of Hydrodynamic and Hydraulic Engineering,
2800 Lyngby, Denmark

This study deals with turbulent oscillatory boundary-layer flows over both smooth and rough beds. The free-stream flow is a purely oscillating flow with sinusoidal velocity variation. Mean and turbulence properties were measured mainly in two directions, namely in the streamwise direction and in the direction perpendicular to the bed. Some measurements were made also in the transverse direction. The measurements were carried out up to $Re = 6 \times 10^6$ over a mirror-shine smooth bed and over rough beds with various values of the parameter a/k_s covering the range from approximately 400 to 3700, a being the amplitude of the oscillatory free-stream flow and k_s the Nikuradse's equivalent sand roughness. For smooth-bed boundary-layer flows, the effect of Re is discussed in greater detail. It is demonstrated that the boundary-layer properties change markedly with Re. For rough-bed boundary-layer flows, the effect of the parameter a/k_s is examined, at large values $(O(10^3))$ in combination with large Re.

1. Introduction

Turbulent oscillatory boundary-layer flows have been the subject of great many investigations for many years. The first experimental work is due to Jonsson (1963). He measured the velocity distributions over a rough boundary and calculated the shear-stress distributions from the measured velocity profiles through the momentum-integral equation.

Various authors have developed theoretical models to cope with the mean-flow properties (such as Kajiura 1968; Bakker 1974 among others), and more recently models have been developed to calculate the turbulence properties of the oscillatory boundary-layer flows (such as Justesen & Fredsøe 1985; Hagatun & Eidsvik 1986; and Justesen 1988 a, b).

Quite recently Spalart & Baldwin (1987) have conducted direct Navier–Stokes simulations of the oscillatory boundary-layer flows over a range of Reynolds numbers (Re) up to 5×10^5 in which Re is defined by

$$Re = \frac{aU_{0m}}{\nu}. \tag{1}$$

U_{0m} is the maximum value of the free-stream velocity, a is the amplitude of the free-stream motion and equal to U_{0m}/ω if the free-stream velocity varies sinusoidally with time (equation (6), and ν is the kinematic viscosity (see figure 1 for the definition sketch).

Although great many works have been devoted to the theoretical investigation of the turbulent oscillatory boundary layers, there are only two major ones that present
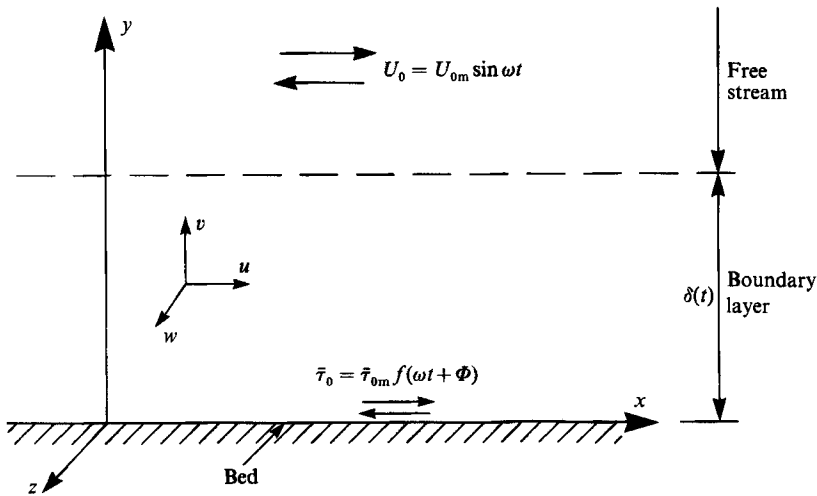
FIGURE 1. Definition sketch.

comprehensive experimental data in connection with both the mean and the turbulence properties of the oscillatory boundary-layer flows: Hino *et al.* (1983) and Sleath (1987). These two works shed considerable light on the understanding of various aspects of turbulence in this kind of boundary-layer flow.

In both studies, the free-stream flow is a purely oscillating flow. In Hino *et al.*'s work the boundary was smooth, while in Sleath's it was covered with sand. Both authors measured the turbulence properties in two directions, namely the streamwise direction and the direction perpendicular to the wall. Figure 2 presents the ranges of turbulence measurements of these two investigations together with the present ones. Here, a/k_s is the roughness parameter, k_s is the Nikuradse's equivalent sand roughness and k_s^+ is the roughness Reynolds number defined by

$$k_s^+ = \frac{k_s U_{fm}}{\nu} \qquad (2)$$

where U_{fm} is the maximum value of the friction velocity.

As far as the smooth-wall oscillatory boundary-layer flows are concerned, the present experiments can be considered to be complementary to Hino *et al.*'s (1983) work in the sense that in the present study attention is concentrated on high-Reynolds-number flows, bearing in mind that Hino *et al.*'s Re value lies well inside the transitional flow regime, as will be seen later in the paper.

As for the rough-wall oscillatory boundary-layer flows, Sleath's (1987) extensive experimental program covers quite a wide range of a/k_s values. Although there are two tests in Sleath's study that correspond to large values of a/k_s ($a/k_s \approx 1000$), the boundary in these tests did not behave quite as a completely rough boundary (since their k_s^+ values lie around 10, as is seen from figure 2), therefore there has been a need to conduct measurements with large a/k_s and k_s^+ values (i.e. at high Re). The present rough-bed experiments were designed to fill this gap, and therefore they can be considered to be complementary to Sleath's (1987) work in that sense.

One other point regarding the large a/k_s oscillatory boundary-layer experiments concerns their direct application to wave boundary layers in the sea. Under storm conditions in the sea, the bed is usually rough and covered by sand. Further it is plane at large values of the Shields' parameter whereby the parameter a/k_s is in the
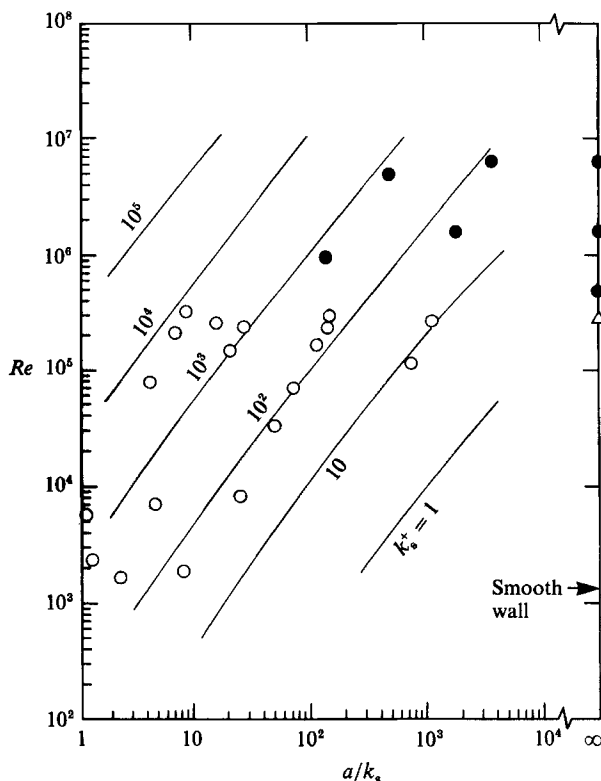
FIGURE 2. Ranges of turbulence measurements conducted by different authors: △, Hino *et al.*
(1983); ○, Sleath (1987); ●, present measurements.

range of 10^3–10^4, in which the roughness is due to the individual sand grains but not
to the bedforms. Considering these facts, the present rough-bed experiments would
be a more realistic representation of the wave boundary layers which occur over the
sea bottom under storm conditions.

2. Experimental set-up

The experiments were carried out in a ∪-shaped oscillatory-flow water tunnel
(figure 3). This tunnel is essentially the same as that described by Lundgren &
Sørensen (1958) and later by Jonsson (1963). The working section was 10 m long and
0.39 m wide. Its height was $H = 0.28$ m in most of the tests of the present study, but
in what will be called the sand-grain-bed experiments the height was $H = 0.30$ m.
The top and side walls of the working section were made of smooth, transparent
Perspex plates. The oscillatory flow in the tunnel was driven by an electronically
controlled pneumatic system. In the tests, the flow was maintained near its resonant
period, which is 9.72 s. The spectra of the velocity at the centreline of the tunnel
indicated that the contributions from the second and third harmonics to the motion
is negligible for all practical purposes (Jensen 1989).

The velocity distribution in the boundary layer over the bottom wall of the tunnel
was measured for three different beds. These consisted of a smooth bed and two
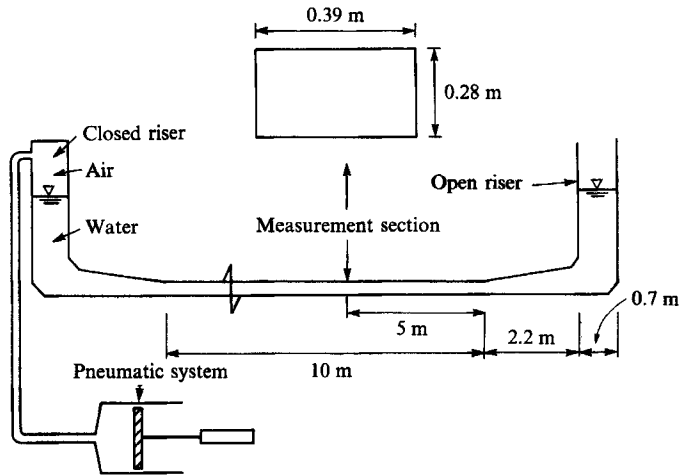rough beds. For the smooth-bed tests PVC plates were fixed rigidly to the bottom of
the tunnel.

FIGURE 3. Schematic description of test set-up.

One of the rough beds of the tests was achieved by gluing a sheet of sandpaper on the bed. The roughness height of the sand paper was measured to be $k = 0.35$ mm, and the density of the protrusions was 80 grains/cm². This resulted in a Nikuradse's equivalent sand-roughness value of $k_s = 0.84$ mm (see §3). The other rough bed, which has been described in Sumer, Jensen & Fredsøe (1987), was obtained directly by gluing sand of fairly uniform size one layer deep to the actual bottom of the tunnel. The roughness height of this wall was measured to be $k = 1.5$ mm. Its k_s value was found to be 2.6 mm for Test 14 and 3.7 mm for Test 15 (see table 1 and §3). Figure 4 presents close-up photographs of the two rough beds.

The velocities were measured by laser-Doppler anemometer (LDA). Two LDA systems were used in the measurements: a one-component system and a two-component system. The former was a Dantec LDA 04 System with a 15 mW He–Ne laser, which was used in forward-scatter mode. The system was equipped with a Dantec 55N10 frequency shifter and a Dantec 55N20 frequency tracker. The two-component system, on the other hand, was a Dantec two-colour high-performance fibre-optic LDA system with a Dantec 60 × 11 fibre-optic probe head. A 100 mW argon laser was used in forward scatter mode with two Dantec 55N10 frequency shifters and two Dantec 55N20 frequency trackers. To minimize the mismatch of the two pairs of laser beams in the two-component velocity measurements, the optic was rotated such that the planes formed by each pair of the beams were at 45° to the flow direction.

The bed shear stress was measured with a Dantec 55R46 hot-film probe. These measurements were conducted only with the smooth bed. The probe was mounted flush to the bed in the middle of the working section. The one-component LDA system was used to monitor the free-stream velocity at the centreline of the tunnel simultaneously with the bed shear stress measurements. In order to ensure correct calibration, the shear-stress probe was calibrated in position. The calibration coefficients A and B in the calibration relation

$$\tau_0^{\frac{1}{3}} = AE^2 + B \qquad (3)$$

were determined in laminar boundary-layer flows where the theoretical solution for the bed shear stress τ_0 is known (equation (11)). Here E is the voltage drop. For

Test no.	Period (s)	U_{0m} (m/s)	a (m)	$Re = aU_{0m}/\nu$	k (mm)	k_s (mm)	a/k_s	U_{fm} (cm/s) Direct meas.	U_{fm} (cm/s) From log fit	$k_s^+ = k_s U_{fm}/\nu$	Quantity measured	Apparatus	Number of cycles sampled	Sampling interval (ms)
									Smooth bed					
1	9.72	0.073	0.113	7.5×10^3	—	—	—	0.77	—	—	$\bar{\tau}_0$, $(\overline{\tau_0'^2})^{\frac{1}{2}}$	Hot film	50	24
2	9.72	0.152	0.235	3.3×10^4	—	—	—	1.1	—	—	$\bar{\tau}_0$, $(\overline{\tau_0'^2})^{\frac{1}{2}}$	Hot film	50	24
3	9.72	0.23	0.36	7.5×10^4	—	—	—	1.4	—	—	$\bar{\tau}_0$, $(\overline{\tau_0'^2})^{\frac{1}{2}}$	Hot film	50	24
4	9.72	0.34	0.53	1.6×10^5	—	—	—	1.7	—	—	$\bar{\tau}_0$, $(\overline{\tau_0'^2})^{\frac{1}{2}}$	Hot film	50	24
5	9.72	0.45	0.70	2.9×10^5	—	—	—	2.3	—	—	$\bar{\tau}_0$, $(\overline{\tau_0'^2})^{\frac{1}{2}}$	Hot film	50	24
6	9.72	0.60	0.94	5×10^5	—	—	—	—	3.2	—	$\bar{u}$, $(\overline{u'^2})^{\frac{1}{2}}$, $(\overline{v'^2})^{\frac{1}{2}}$, $\overline{u'v'}$	Two-Comp. LDA	80	24
7	9.72	0.68	1.05	6.5×10^5	—	—	—	3.5	—	—	$\bar{\tau}_0$, $(\overline{\tau_0'^2})^{\frac{1}{2}}$	Hot film	50	24
8	9.72	1.02	1.58	1.6×10^6	—	—	—	4.8	4.9	—	$\bar{\tau}_0$, $(\overline{\tau_0'^2})^{\frac{1}{2}}$ $\bar{u}$, $(\overline{u'^2})^{\frac{1}{2}}$, $(\overline{v'^2})^{\frac{1}{2}}$, $\overline{u'v'}$	One-Comp. LDA Two-Comp. LDA	80 80	24 48
9	9.72	1.55	2.4	3.4×10^6	—	—	—	6.4	—	—	$\bar{\tau}_0$, $(\overline{\tau_0'^2})^{\frac{1}{2}}$	Hot film	50	24
10	9.72	2.0	3.1	6×10^6	—	—	—	7.7	8.0	—	$\bar{\tau}_0$, $(\overline{\tau_0'^2})^{\frac{1}{2}}$ $\bar{u}$, $(\overline{u'^2})^{\frac{1}{2}}$ $\bar{u}$, $(\overline{u'^2})^{\frac{1}{2}}$, $(\overline{v'^2})^{\frac{1}{2}}$, $\overline{u'v'}$	Hot film One-Comp. LDA Two-Comp. LDA	50 80 80	24 24 48
11	9.72	2.0	3.1	6×10^6	—	—	—	—	8.0	—	$\bar{u}$, $(\overline{u'^2})^{\frac{1}{2}}$, $(\overline{v'^2})^{\frac{1}{2}}$, $\overline{u'v'}$, $(\overline{w'^2})^{\frac{1}{2}}$	Two-Comp. LDA	80	48
							Rough bed with $k = 0.35$ mm sand paper							
12	9.72	1.02	1.58	1.6×10^6	0.35	0.84	1880	—	5.8	44	$\bar{u}$, $(\overline{u'^2})^{\frac{1}{2}}$ $\bar{u}$, $(\overline{u'^2})^{\frac{1}{2}}$, $(\overline{v'^2})^{\frac{1}{2}}$, $\overline{u'v'}$	One-Comp. LDA Two-Comp. LDA	80 80	24 48
13	9.72	2.00	3.1	6×10^6	0.35	0.84	3700	—	11.0	84	$\bar{u}$, $(\overline{u'^2})^{\frac{1}{2}}$ $\bar{u}$, $(\overline{u'^2})^{\frac{1}{2}}$, $(\overline{v'^2})^{\frac{1}{2}}$, $\overline{u'v'}$	One-Comp. LDA Two-Comp. LDA	80 80	24 48
							Rough bed with $k = 1.5$ mm sand grains							
14	8.12	0.87	1.13	9×10^5	1.5	2.6	435	—	6.0	142	$\bar{u}$, $(\overline{u'^2})^{\frac{1}{2}}$	One-Comp. LDA*	50	14
15	8.12	2.1	2.71	5.2×10^6	1.5	3.7	730	—	14.0	460	$\bar{u}$, $(\overline{u'^2})^{\frac{1}{2}}$	One-Comp. LDA*	50	14

TABLE 1. Test conditions. ν is 1.14×10^{-2} cm²/s in all tests. The dimensions of the measuring volume ($d_x \times d_y \times d_z$) are 0.3 mm × 0.3 mm × 3.2 mm for One-Comp. LDA, 0.15 mm × 0.15 mm × 2.5 mm for Two-Comp. LDA (except Test 11) and 0.6 mm × 0.6 mm × 12.0 mm for One-Comp. LDA*. $d_x \times d_z$ for the Hot-Film = 0.2 mm × 0.75 mm. In Test 11, w was measured in the boundary layer over the sidewall of the water tunnel. $d_x \times d_y \times d_z$ = 0.15 mm × 2.5 mm × 0.15 mm.
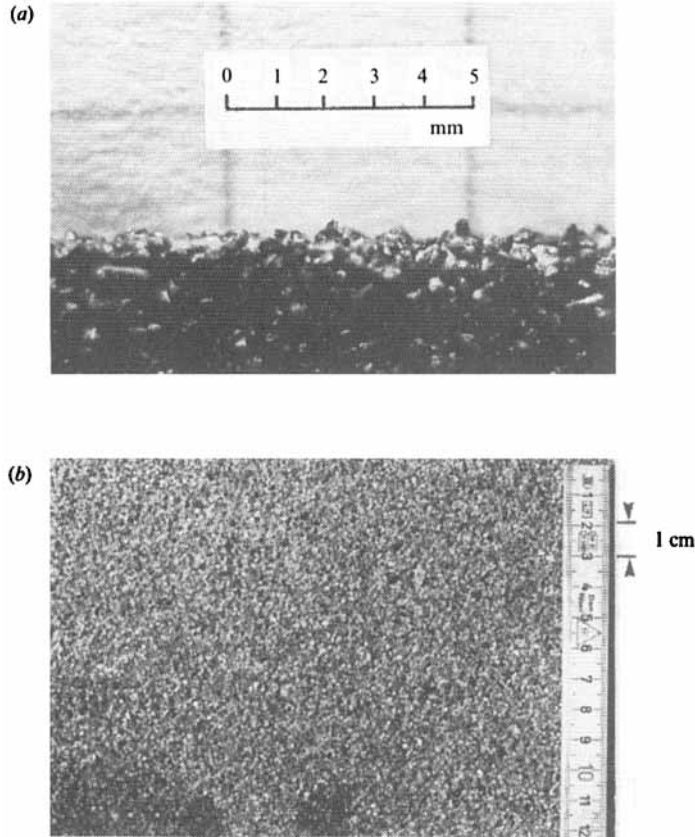
FIGURE 4. Close-up photographs of the rough beds of the present tests: (a) sandpaper and (b) sand.

turbulent flows, (3) (with the coefficients A and B determined from laminar-flow experiments) holds true provided that τ_0 is the instantaneous value of the wall shear stress and E the corresponding instantaneous voltage drop (Hanratty & Campbell 1983).

Using a wave gauge, the water level in the open riser of the U-tube was recorded simultaneously with the velocity measurements. This served as a reference signal in data processing.

The measurements were made at sampling intervals of 14 and 48 ms, the former being the sampling interval for the tests done with the sand-grain-bed roughness (see table 1). These values correspond to approximately 600 and 200 samples per cycle, respectively. These latter values are large enough to be able to trace the time evolution of the measured statistical quantities over the flow period. Figure 5 shows sample velocity records, the top record representing the free-stream velocity and the bottom ones the u- and the v-velocity components (see definition sketch in figure 1) in the boundary layer, while figure 6 shows sample records of the free-stream velocity and the bed shear stress.

Mean values of the quantities are calculated through ensemble averaging according to

$$\bar{\phi}(y, \omega t) = \frac{1}{N} \sum_{j=1}^{N} \phi[y, \omega(t + (j-1)\,T)], \qquad (4)$$
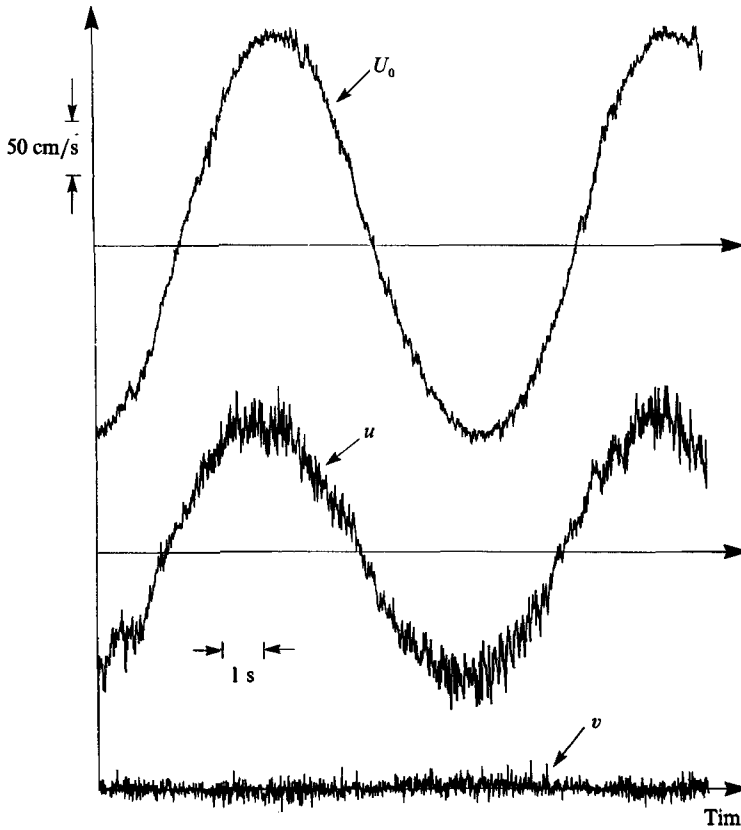
50 cm/s

U_0

u

1 s

v

Time

FIGURE 5. Sample velocity records. $Re = 6 \times 10^6$. U_0 was measured at $y = 140$ mm, and u and v at $y = 1$ mm. Test 10.

where ϕ is the quantity in consideration, y the distance from the bed, ω the angular frequency of the oscillatory flow, t the time and T the period of the oscillatory flow. The root-mean-square (r.m.s.) value of the fluctuating component of ϕ, $\phi' = \phi - \bar{\phi}$, is calculated by

$$(\overline{\phi'^2})^{\frac{1}{2}}(y, \omega t) = \left\{ \frac{1}{N-1} \sum_{j=1}^{N} (\phi[y, \omega(t+(j-1)T] - \bar{\phi}(y, \omega t))^2 \right\}^{\frac{1}{2}}. \tag{5}$$

The total number of cycles sampled was $N = 50$ for the sand-grain-bed experiments and for the bed-shear-stress tests, while $N = 80$ for the other tests. Sleath (1987) reported that, for record lengths larger than about $N = 50$, no significant improvement in the consistency of the statistics was obtained with increase in the number of cycles sampled. Indeed the tests carried out in the present study confirmed Sleath's finding.

3. Test conditions

Table 1 summarizes the test conditions for the measurements: u, v and w are the flow velocities in the x-, y- and z-directions, respectively (figure 1), U_{0m} is the maximum value of the free-stream velocity defined by
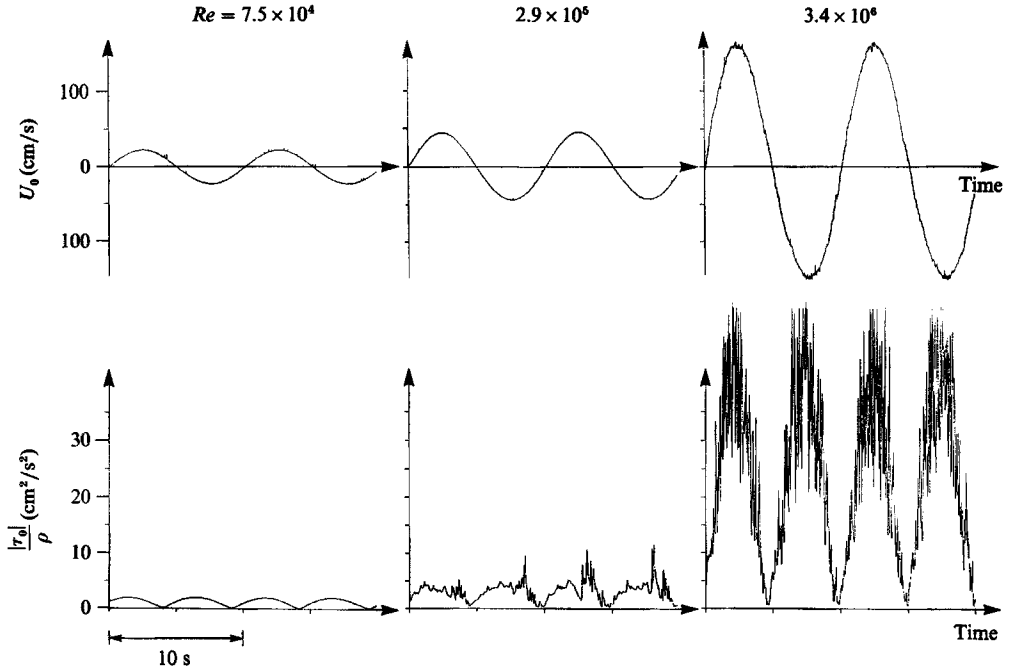
$$U_0 = U_{0m} \sin \omega t, \tag{6}$$

FIGURE 6. Sample records of free-stream velocity and bed shear stress. Smooth bed.
Tests 3, 5 and 9.

τ_0 is the bed shear stress and U_{fm} is the maximum bed shear-stress velocity defined by

$$U_{fm} = \left(\frac{\bar{\tau}_{0m}}{\rho}\right)^{\frac{1}{2}} \tag{7}$$

where ρ is the fluid density and $\bar{\tau}_{0m}$ is the maximum value of the mean bed shear stress $\bar{\tau}_0$,

$$\bar{\tau}_0 = \bar{\tau}_{0m} f(\omega t + \Phi), \tag{8}$$

where Φ is the phase lead of the maximum shear stress $\bar{\tau}_{0m}$ over the maximum value of the free-stream velocity U_{0m}, and f is a periodic function of time, and generally dependent on Reynolds number and the bed roughness.

In the smooth-bed experiments, U_{fm} was obtained by (i) direct measurements of the bed shear stress as described in the previous section and (ii) by fitting straight lines to the logarithmic-layer portion of the mean velocity distribution for those tests where the velocity distribution was measured.

In the rough-bed experiments, on the other hand, U_{fm} was determined only by the latter method. This method gave also the Nikuradse's equivalent sand roughness k_s. The values of k_s indicated in table 1 are those obtained in this way. Figure 7 presents the bed shear velocity

$$U_f = \left(\frac{\bar{\tau}_0}{\rho}\right)^{\frac{1}{2}} \tag{9}$$

obtained by the latter method plotted against the phase variable ωt.

Note that the largest amplitude in the table is 3.1 m. That means that the total travel of a fluid particle in this case is 6.2 m, implying that some fluid in the core
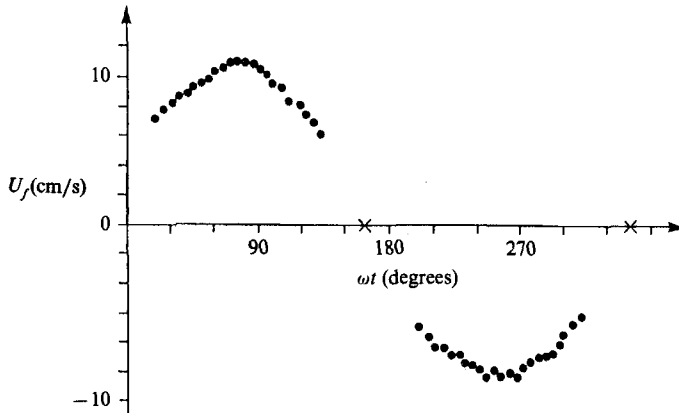
FIGURE 7. Friction velocity: ●, logarithmic fit; ×, $\bar{u}$ measurements, representing the instant where the near-bed-flow reverses. Test 13.

region of the tunnel travels outside the straight 10 m working section and then returns to the measurement section at the end of one period. To check whether this is a problem, additional mean velocity and turbulence measurements were conducted at several x-stations at the distance $y = 1$ cm and at the centreline of the tunnel. These measurements indicated that no 'contamination' can be traced in the neighbourhood of the measured section, caused by this effect (Jensen 1989).

4. Smooth wall

4.1. *Laminar-to-turbulent transition*

One way of illustrating the laminar-to-turbulent transition is to plot the friction coefficient as function of Reynolds number. Figure 8 presents such a plot for the present smooth-bed experiments where the temporal value of the friction coefficient is plotted against Re for various values of the phase ωt, in which the friction coefficient is defined by

$$f_w^* = \frac{2\frac{\bar{\tau}_0}{\rho}/U_{0m}^2}{\cos{(\omega t - \frac{1}{4}\pi)}} \tag{10}$$

The friction coefficient is normalized with the factor $\cos{(\omega t - \frac{1}{4}\pi)}$ so that the laminar-flow points collapse onto one common line, since it is known that the laminar flow solution satisfies the following relation (Batchelor 1967):

$$\tau_0 = \frac{\rho U_{0m}^2}{Re^{\frac{1}{2}}} \cos{(\omega t - \frac{1}{4}\pi)}. \tag{11}$$

Figure 8 shows that every individual phase value experiences three distinct flow states, the laminar, the transitional and the turbulent, as Re is increased. Secondly, the figure indicates that the transition does not occur abruptly. For example, for $\omega t = 60°$, the transitional-flow state occurs over a range of Re, from 1.5×10^5 to 1×10^6, and it is only after Re reaches the value of 1×10^6 that the flow regime becomes a fully developed turbulent one. Thirdly, it is seen that the Re range over which the transitional flow occurs constantly shifts to higher values of Re number, as ωt decreases.
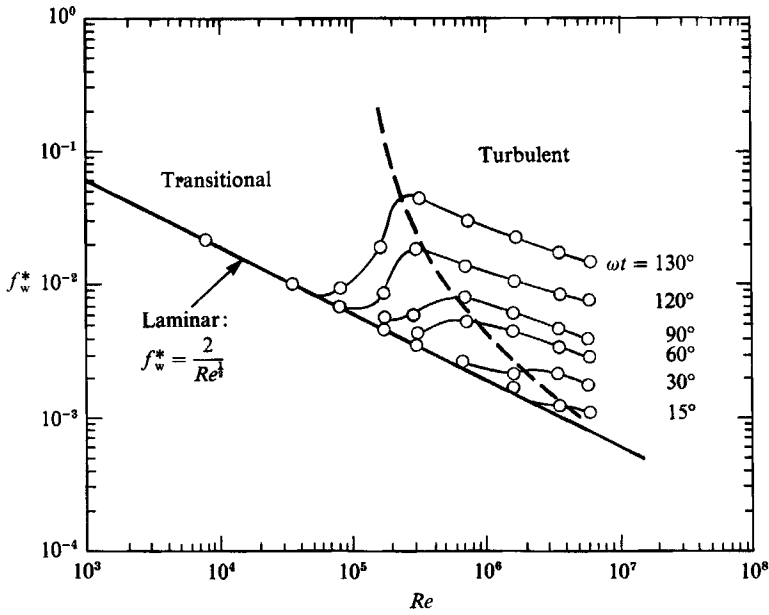
FIGURE 8. Normalized friction coefficient versus Re at different phase values. Smooth bed. See (10) for definition f_w^*.
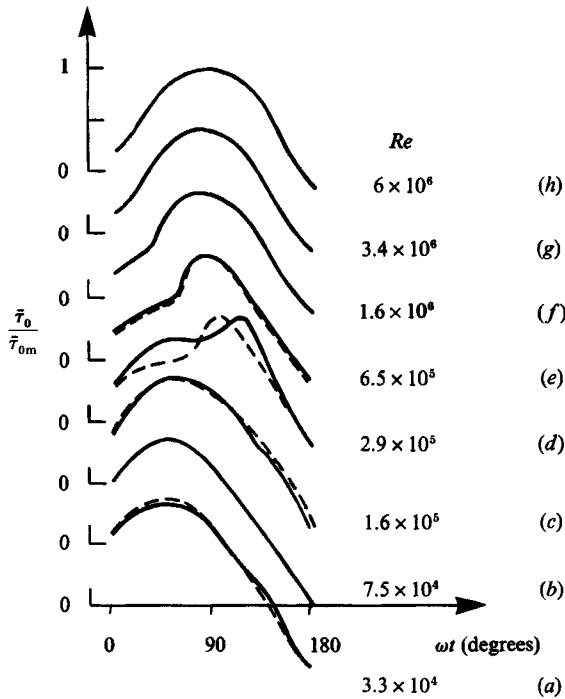

FIGURE 9. Evolution of bed shear stress over one half-cycle for various Re. Smooth bed. Tests 2–10. Dashed curve in (a), equation (11). Dashed curves in (c), (d) and (e), direct Navier–Stokes simulation results of Spalart & Baldwin (1987) $(c, Re = 1.8 \times 10^5; d, Re = 3.2 \times 10^5$ and $e, Re = 5 \times 10^5)$.
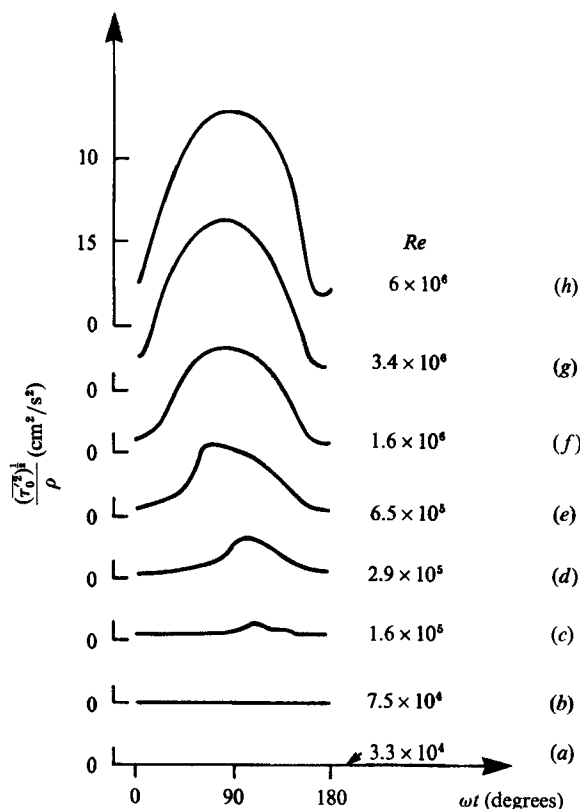
FIGURE 10. Evolution of the r.m.s. value of bed shear stress fluctuations over one half-cycle for various *Re*. Smooth bed. Tests 2–10.

Figure 9 depicts the present skin-friction measurements plotted in such a way that the phase evolution of the mean bed shear stress can be traced. Also plotted in the figure are the available Navier–Stokes solutions for comparison. The one corresponding to $Re = 3.3 \times 10^4$ is the laminar flow solution given in (11). The rest are those obtained through the direct Navier–Stokes simulation method presented in Spalart & Baldwin (1987). The skin friction is normalized with τ_{0m} to facilitate comparison with this latter work. As is seen from the figure, the agreement between the experiments and the theoretical solutions is good. Although no clear explanation has been found for the discrepancy in figure 9(c), this may be attributed to the difference in Re, since the shear-stress pattern in this particular subrange of Re is fairly sensitive to the change in Re.

Figure 10 presents the phase evolution of the r.m.s. value of the fluctuations in the bed shear stress for the same Re as in figure 9.

From figures 9 and 10, it is remarkable how the bed shear-stress profiles deform as we proceed through the Re range. The laminar shear-stress profile is disturbed first at $Re = 1.6 \times 10^5$, thus the bed-shear-stress experiences turbulence first at this value. This occurs just prior to the bed shear-stress reversal. This is not surprising, because the adverse pressure gradient becomes relatively large and the velocity of near-bed fluid particles becomes relatively small at this phase value so that a very favourable environment forms for the initiation of turbulence.

It is seen from figures 9 and 10 that the occurrence of turbulence in the bed shear
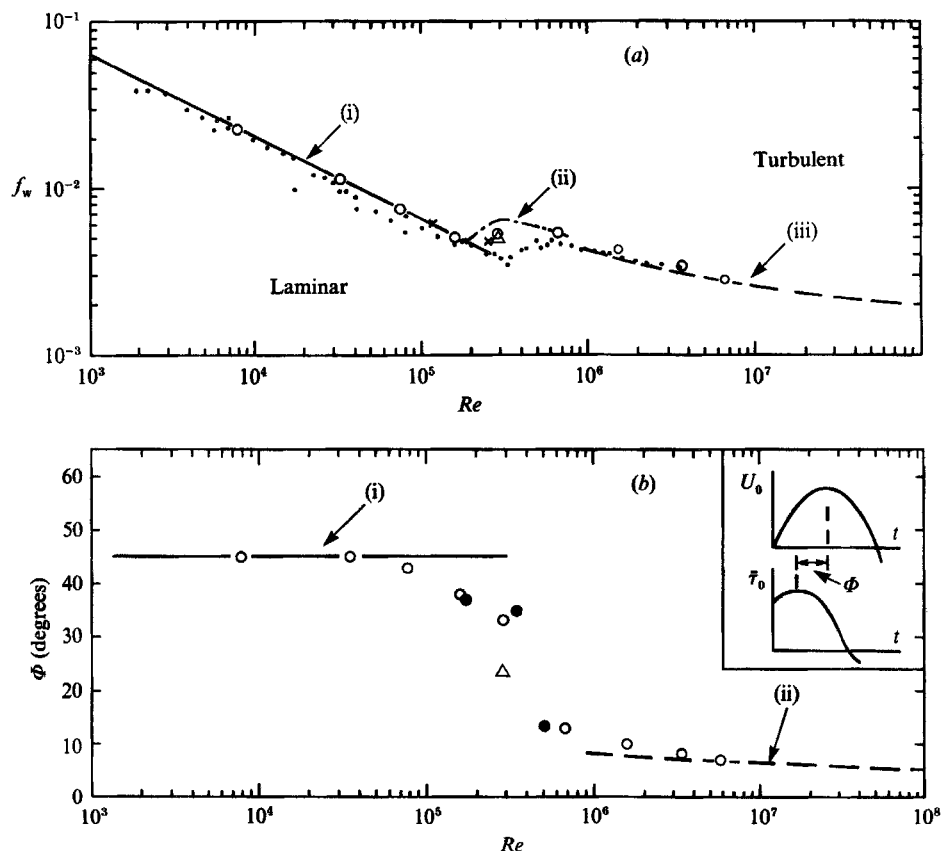
FIGURE 11 (a) Wave friction coefficient versus Re. Smooth bed. See (12) for definition of f_w. (i) Laminar, $f_w = 2/Re^{\frac{1}{2}}$; (ii) Spalart & Baldwin's (1987) direct Navier–Stokes simulation; (iii) Fredsøe's theoretical (1984) solution; $\bigcirc$, present experiments; $\bullet$, Kamphuis's (1975) experiments; $\triangle$, Hino et al.'s (1983) experiment; $\times$, Sleath's (1987) 0.2 mm sand bed test where $k_s^+ \approx 10$. (b) Phase lead of the maximum bed shear stress over the maximum free-stream velocity. (i) Laminar; (ii) Fredsøe's (1984) theoretical solution; $\bullet$, Spalart & Baldwin's (1987) direct Navier–Stokes simulation; $\bigcirc$, present experiments; $\triangle$, Hino et al.'s (1983) experiment.

stress spreads towards the lower values of phase ωt, as Re is increased (figures 9c, d, e and 10c, d, e). Once it has reached the acceleration stage (i.e. $\omega t < \frac{1}{2}\pi$), further spreading of turbulence to lower values of ωt with increasing Re is resisted by the presence of the favourable pressure gradient, which is a characteristic feature of the acceleration stage (figures 9e, f, g and 10e, f, g). This explains why the transition to the fully developed turbulent flow regime (observed in figure 8) is delayed and cannot be completed for a very wide range of Re.

The present observations reveal most of the transition features shown by the earlier velocity measurements of Hino, Sawamoto & Takasu (1976) conducted in a pipe flow.

As mentioned previously, turbulence first occurs just prior to the phase where the bed shear stress reverses, namely at $\omega t \approx 135°$. From this information and from the friction-factor diagram in figure 8, it can be deduced that the critical value of Re corresponding to the first appearance of turbulence is $Re_{cr} \approx 10^5$. This value appears to be in fairly good agreement with the experimental data reported in the literature
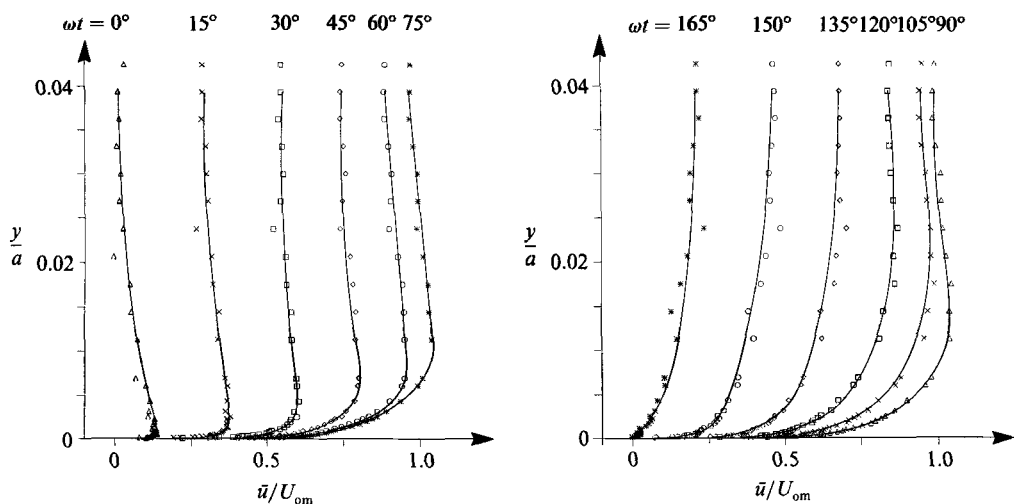
FIGURE 12. Mean velocity distributions. Smooth bed, $Re = 6 \times 10^6$. Test 10.
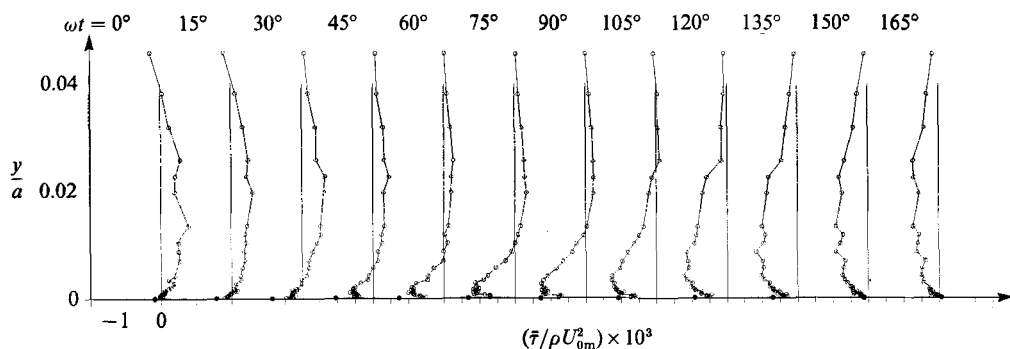
FIGURE 13. Shear-stress distributions. Smooth bed. $Re = 6 \times 10^6$. Test 10. $\bigcirc$, $\bar{\tau} = -\rho\overline{u'v'} + \mu\, \partial\bar{u}/\partial y$; $\bullet$, direct measurements of $\bar{\tau}$ at the wall.

(see for example Sleath 1984) and also with the value 1.58×10^5 obtained by a stability analysis (again see Sleath 1984).

The maximum bed shear stress is the key quantity (as far as the bed shear stress is concerned) when the analysis of wave boundary layers is considered. The corresponding friction coefficient is defined by

$$f_{\rm w} = 2\frac{\bar{\tau}_{\rm 0m}}{\rho}/U_{\rm 0m}^2. \tag{12}$$

This friction coefficient along with the corresponding phase information is plotted in figure 11 together with the available experimental data and theoretical solutions. The fully developed turbulent boundary-layer solution shown in the figure is due to Fredsøe (1984) and obtained by the integration of the momentum equation, while the transitional flow solution is due to Spalart & Baldwin (1987) and obtained by the direct Navier–Stokes simulation method, as mentioned previously. It is seen that there is a general agreement between the present results and the experimental results of the other authors. Further, the present results appear to be in good agreement with the theoretical solutions given in the figure.
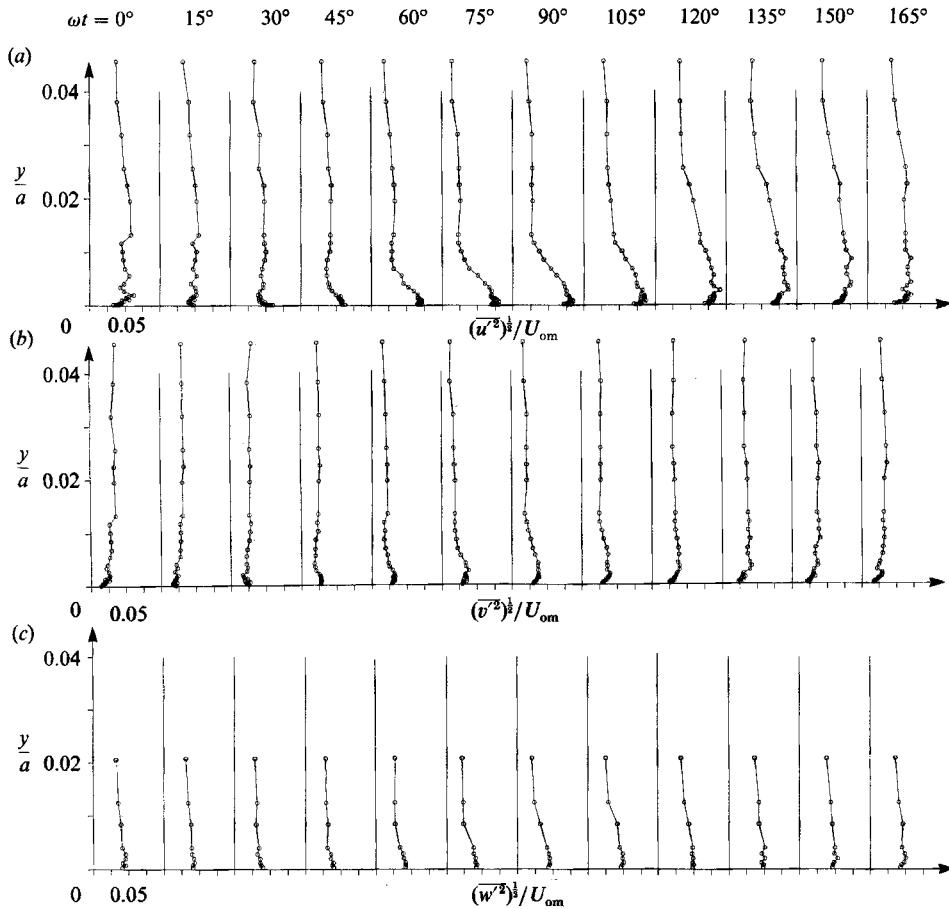
FIGURE 14. Distributions of r.m.s. values of velocity fluctuations u', v' and w'. Smooth bed, $Re = 6 \times 10^6$. (a) and (b) Test 10, (c) Test 11.

4.2. Fully-developed turbulent flow

In this section, the data obtained in Tests 10 and 11 where $Re = 6 \times 10^6$ will be presented. The presentation will be made in normalized forms, first using the outer-flow parameters U_{0m} and a, and then the inner-flow parameters $U_f((\bar{\tau}_0/\rho)^{\frac{1}{2}})$ and ν, as the scaling parameters. In the normalization made with the outer-flow parameters, the boundary-layer thickness is abandoned in favour of the flow amplitude a, simply to avoid the uncertainty involved in the experimental determination of the boundary-layer thickness.

Figure 12 gives the mean velocity profiles at different phase values, figure 13 presents the corresponding shear-stress profiles, while figure 14 gives the profiles of the r.m.s. values of u', v' and w'.

Figures 13 and 14 illustrate how the turbulence evolves as the flow progresses in phase space: (i) the turbulence builds up near the bed and constantly diffuses away from the bed across the boundary layer, as the boundary layer develops in time; (ii) by the time of approximately $\omega t = 140°$, the near-bed build-up of turbulence almost comes to an end; and (iii) the turbulence becomes almost uniformly distributed across the depth, as the time of free-stream flow reversal is reached.

Figures 15–17 present the $Re = 6 \times 10^6$ test data in terms of the inner-flow parameters. There are two advantages of the inner-flow representation; (i) it gives a better picture of the boundary-layer behaviour close to the bed; (ii) the fact how the oscillatory boundary layer relates to the familiar steady boundary layer could possibly be best explained by reference to the inner-flow representation.

Figure 15 gives the mean velocity profiles at different phase values, where $\bar{u}^+ = \bar{u}/U_f$ and $y^+ = yU_f/\nu$. Also plotted in the figure is the steady boundary-layer velocity distribution which is valid close to the wall

$$\bar{u}^+ = 2 \int_0^{y^+} \frac{\mathrm{d}y^+}{1 + \{1 + 4\kappa^2 y^{+2}[1 - \exp(-y^+/A)]^2\}^{\frac{1}{2}}} \tag{13}$$

where κ is the von Kármán constant ($= 0.4$) and A the van Driest damping factor ($= 25$) (van Driest 1956). Note that $\bar{u}^+$ tends to the logarithmic distribution $\bar{u}^+ = (1/\kappa)\ln y^+ + 5$ for large values of y^+, as seen from the figure (the dashed lines).

Figure 15 shows that the oscillatory-flow velocity distributions agree remarkably well with the steady-flow ones in the range of ωt from 70° to 110° where the flow experiences almost zero pressure gradient. The figure also indicates that the logarithmic layer exists already at $\omega t = 15°$ and is maintained throughout the ωt-range, from $\omega t \approx 15°$ up to almost 160° where the near-bed flow reversal takes place (see figure 12). At the earlier phases the logarithmic layer does not exist, however. This is simply because the boundary layer at these stages is not thick enough to house the logarithmic layer in it. It is also noticed that the distributions corresponding to the early phases of the acceleration stage (where the pressure gradient is favourable) resemble quite closely the velocity distributions obtained in favourable pressure-gradient steady boundary layers. Likewise, the velocity distributions in the later phases of the deceleration stage resemble, again, quite closely the velocity distributions obtained in adverse-pressure-gradient steady boundary layers (Coles 1956).

Figures 16 and 17 present the turbulence data in terms of inner-flow parameters, where $u'^+ = (\overline{u'^2})^{\frac{1}{2}}/U_f, v'^+ = (\overline{v'^2})^{\frac{1}{2}}/U_f, w'^+ = (\overline{w'^2})^{\frac{1}{2}}/U_f$ and $\overline{u'v'}^+ = \overline{u'v'}/U_f^2$. Also plotted in the figures are the known steady boundary-layer distributions (the solid curves) for comparison (see for example Spalart 1988).

Figure 16(*a*) gives the r.m.s. u' profiles. The dashed line in the figure represents the line tangent to the curve $u'^+(y^+)$ at $y = 0$. It was obtained from direct measurements of the bed shear stress (figure 10) through the equation

$$\overline{\tau_0'^2} = \mu^2 \frac{\partial \overline{u'^2}}{\partial y}. \tag{14}$$

Since the velocities could not be measured very close to the bed (for y-values of $O(0.3 \text{ mm})$) owing to the experimental constraints involved, plotting of the previously mentioned tangent lines is quite advantageous, as they will illustrate how the r.m.s. values of u' are distributed very close to the bed.

Except at very early stages of the acceleration phase and also late stages of the deceleration phase, the u'^+ profiles appear to be in reasonable accord with the steady boundary-layer distribution throughout the phase space. The slightly underpredicted values of u'^+ in the acceleration stage and the slightly overpredicted values of u'^+ in the deceleration stage may be attributed to the history effect where the response of $\overline{u'^2}$ to the wall quantity U_f is not instantaneous.
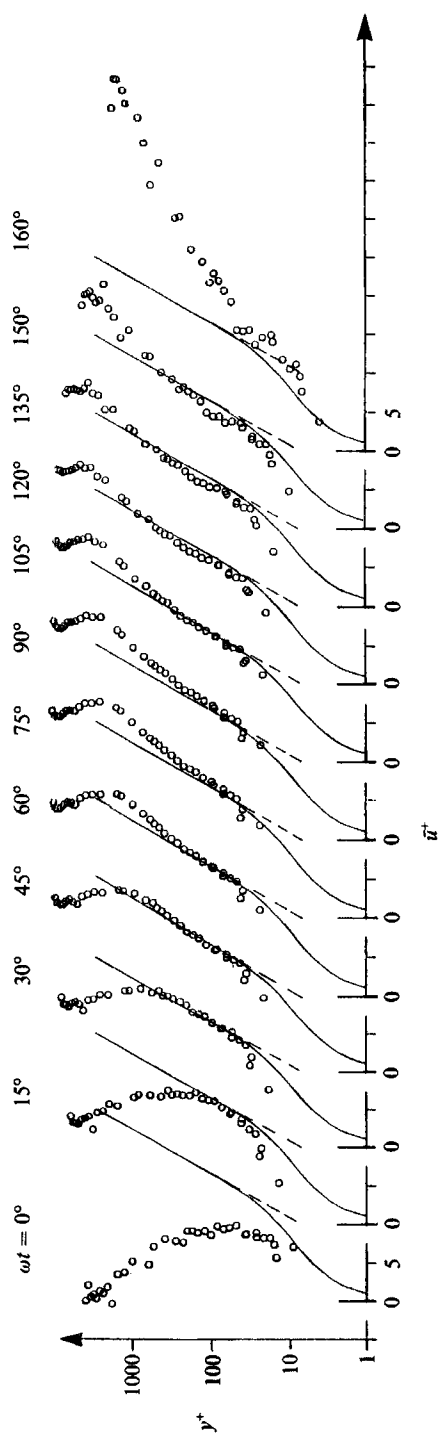
FIGURE 15. Mean velocity distributions in semi-log plot. Smooth bed, $Re = 6 \times 10^6$. Test 10.
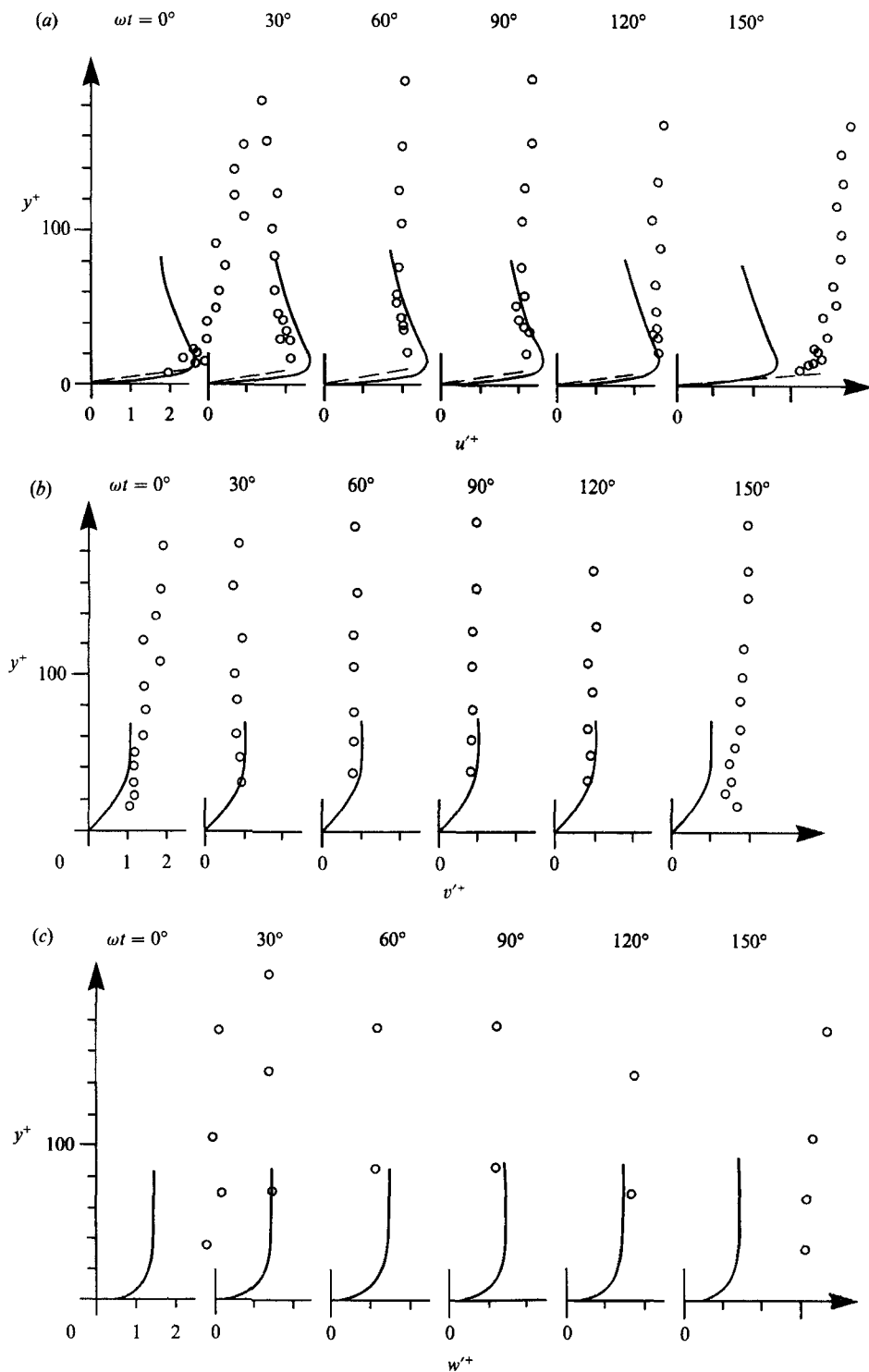Solid curve, equation (13). Dashed lines, log law.

FIGURE 16. R.m.s. values of (a) u', (b) v' and (c) w' normalized with inner-flow parameters. Smooth bed, $Re = 6 \times 10^6$. Test 10. Solid curve, steady boundary-layer distributions; $\bigcirc$, present experiments; Dashed line, from direct measurements of wall shear stress, obtained from (14).
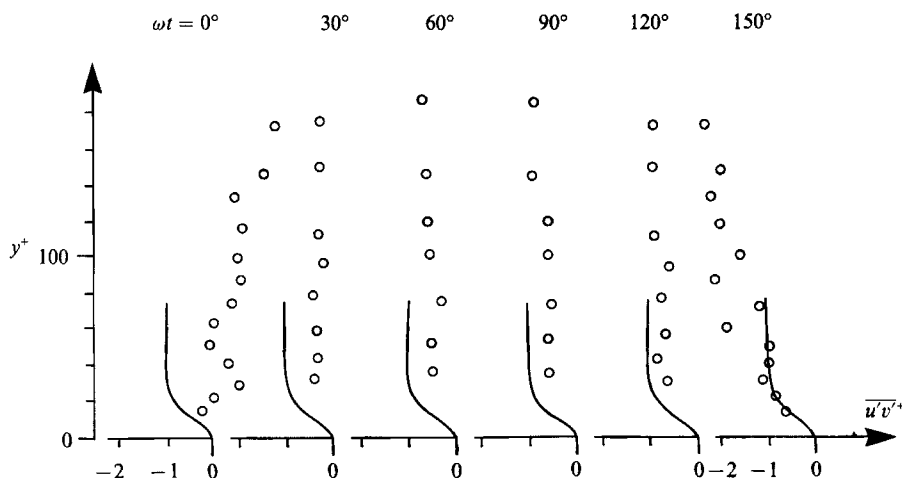
FIGURE 17. Reynolds stress normalized with inner-flow parameters. Smooth bed, $Re = 6 \times 10^6$. Test 10. Solid curve, steady boundary-layer distributions; ◯, present experiments.

Figures 16(b) and 16(c) give the r.m.s. v' and r.m.s. w' profiles. The same arguments given above for the u'^+ component apply also for v'^+ and w'^+.

Figure 17 gives the Reynolds-stress profiles normalized with the inner-flow parameters. One would expect that, for phases $\omega t \sim \frac{1}{2}\pi$, the Reynolds-stress profiles obtained for oscillatory boundary layers should approach that for steady boundary-layer flows. From figure 17, however, it seems that this is the case only for locations away from the bed. The discrepancy between the measured values of the Reynolds stresses near the wall and the expected value $\overline{u'v'} = U_f^2$, where U_f is obtained from direct measurements was found to be due to a high drop-out rate in the laser measurements in the region very close to the wall. The correlation coefficient $R = \overline{u'v'}/(\overline{u'^2})^{\frac{1}{2}}(\overline{v'^2})^{\frac{1}{2}}$ in the region up to $y = 1$–2 mm took the value of 0.25–0.3 where the expected value would be around 0.5.

The drop-out was caused by the disturbing effect of the laser light reflected by the smooth wall surface. This belief was supported by the fact that an experiment where the drop-out rate was higher because no artificial seeding material was added to the fluid, caused the correlation to drop to an even lower value of 0.1–0.2, while both $(\overline{u'^2})^{\frac{1}{2}}$ and $(\overline{v'^2})^{\frac{1}{2}}$ were relatively unaffected, and also by the fact that the Reynolds stresses recovered their expected value at y distances bigger than 1–2 mm where practically no drop-outs were found. Also, it should be mentioned that in the case of rough-bed experiments, the measurements of Reynolds stresses were somewhat improved (Jensen 1989). This again supports the argument that the drop-out was caused by the disturbing effect of the laser light reflected by the smooth-wall surface.

Since both the direct determination of U_f, the determination of U_f through the logarithmic profile and finally the extrapolation of the measured values for $y > 2$ mm in figure 13 to the wall, all give identical results, it seems evident that the laser-measured Reynolds stresses near the wall actually are underpredicted. (Note that one of the referees suggested that the underprediction of the Reynolds stresses may have been caused by a very slight difference between the beam intersection points for the two velocity components.)

It should be mentioned that also Sleath (1988) reported unexpectedly low values of laser-measured Reynolds stresses near the wall.
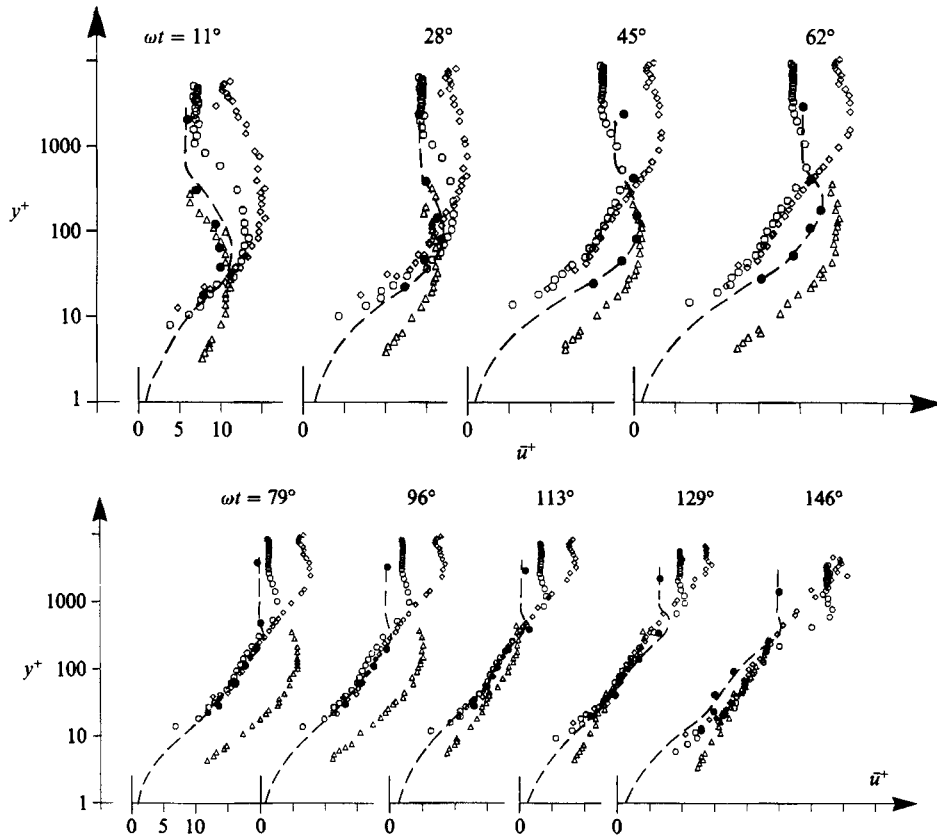
FIGURE 18. Mean velocity distributions in semi-log plot for various Re. Smooth bed. $\Diamond$, $Re = 6 \times 10^6$, Test 10; $\bigcirc$, $Re = 1.6 \times 10^6$, Test 8; $\bullet$, $Re = 5 \times 10^5$, Test 6; Dashed lines, $Re = 5 \times 10^5$, Spalart & Baldwin's (1987) direct Navier–Stokes simulation; $\triangle$, $Re = 2.8 \times 10^5$, Hino *et al.* (1983).

4.3. *Effect of Reynolds number*

Figure 18 gives the velocity profiles for four different Re-values in terms of the inner-flow parameters. Two of them come from the studies of other authors: the profiles corresponding to the lowest Re, namely $Re = 2.8 \times 10^5$, are the ones obtained in Hino *et al.*'s (1983) experiments, while the profiles corresponding to $Re = 5 \times 10^5$ (the dashed lines) are those obtained in Spalart & Baldwin's (1987) direct Navier–Stokes simulation work.

The inner-flow representation is particularly instructive in demonstrating how the velocity profile evolves in phase space for different Re. The characteristic features of this evolution are as follows: (i) the velocity profile eventually reaches a state where the logarithmic layer comes into existence; (ii) this logarithmic layer grows in thickness, as one proceeds further in the ωt-space; and (iii) this continues to be the case until practically the point of flow reversal near the bed is reached.

From figure 18 it is observed that the higher Re, the earlier the logarithmic layer comes into existence. For $Re = 6 \times 10^6$ this occurs at $\omega t \approx 15°$ (as has been mentioned previously; §4.2, see also figure 15), for $Re = 1.6 \times 10^6$ at $\omega t \approx 45°$, for $Re = 5 \times 10^5$ at $\omega t \approx 80°$ and for $Re = 2.8 \times 10^5$ at $\omega t \approx 120°$. This behaviour can be explained by reference to figure 8, from which it can be seen that, for the establishment of the logarithmic layer, the flow has to reach the fully developed turbulent state.
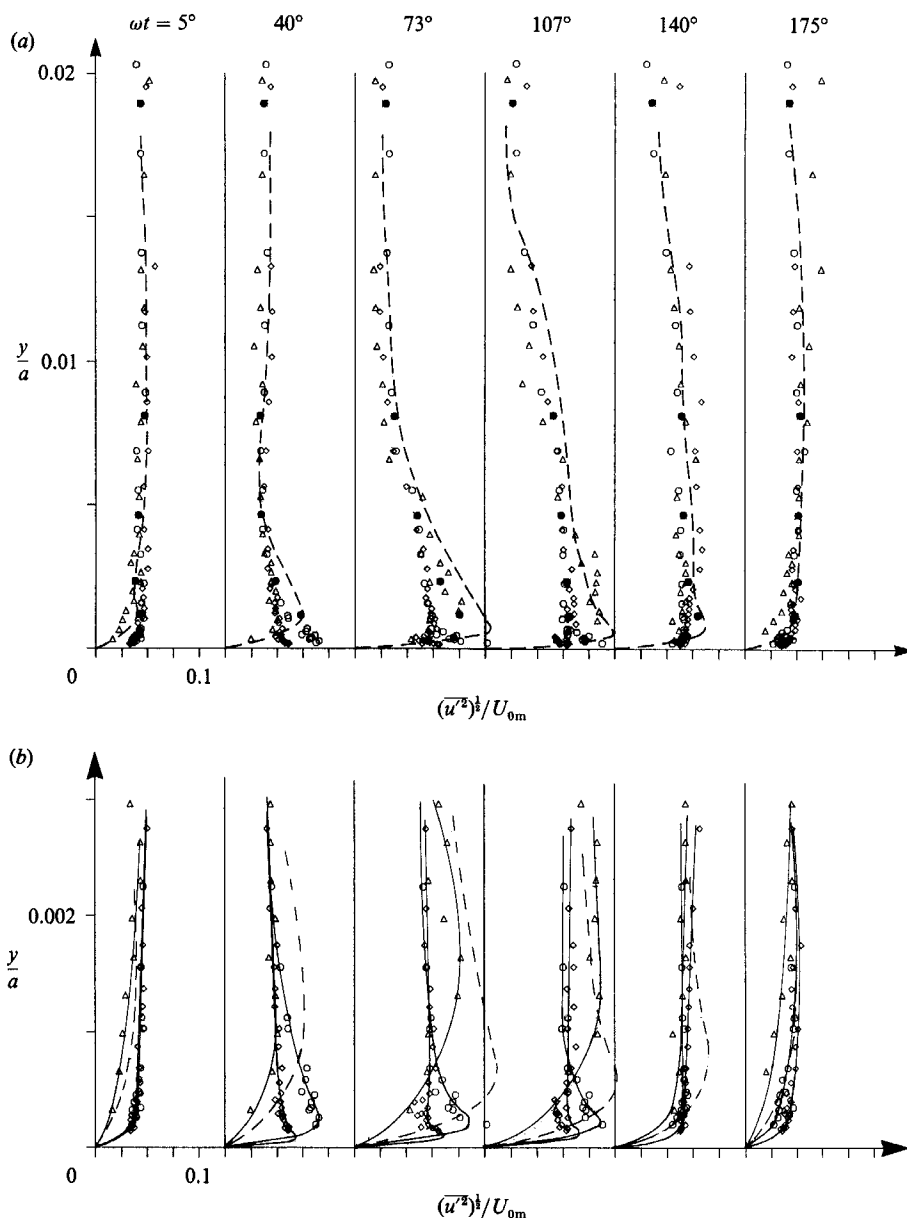
FIGURE 19. R.m.s. value of u' for different Re. Smooth bed. Symbols as figure 18.

It is remarkable to observe from figure 18 how the velocity profile for $Re = 2.8 \times 10^5$ evolves with time. It is only after ωt reaches the value of 120° that the logarithmic distribution, $\bar{u}^+ = 2.5 \ln y^+ + 5$, is established in the velocity profile for this Re. The reason behind this can again be traced from figure 8.

Figures 19, 20 and 21 present the r.m.s. u', the r.m.s. v' and the $\overline{u'v'}$ distributions, respectively, for the same Re as in the previous figure.

From these figures it is seen that there are two distinct flow regions. (i) The region away from the bed where there exists a very weak Re dependence, except for $Re = 2.8 \times 10^5$. Notice that this dependence is so weak that, at places, it is obstructed by
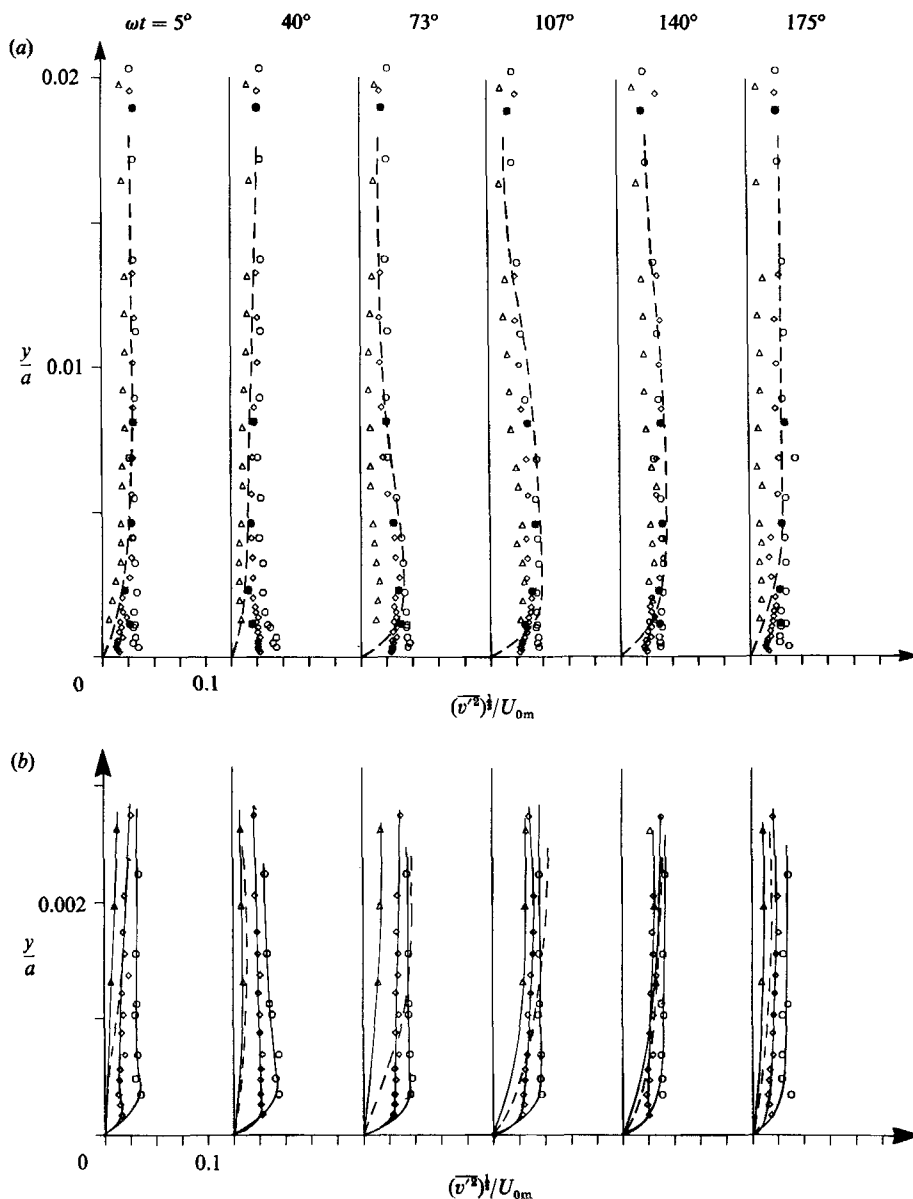
FIGURE 20. R.m.s. value of v' for different Re. Smooth bed. Symbols as figure 18.

the experimental uncertainties. For $Re = 2.8 \times 10^5$, however, the results appear to be distinctly different from those at other Re. This must be attributed to the fact that the flow at this Re experiences the transitional flow regime most of the time during the course of the flow oscillations (figure 8) and, as a result of this, the turbulence properties appear to be distinctly different from those of the other Re cases in figures 19–21. (ii) The region near the bed where there is definitely a marked Re dependence (figures 19b, 20b, 21). This dependence exists even at the Re for which the fully developed turbulent flow regime occurs most of the time during the course of the flow oscillation (figure 8), namely $Re = 6 \times 10^6$, 1.6×10^6 and also 5×10^5.
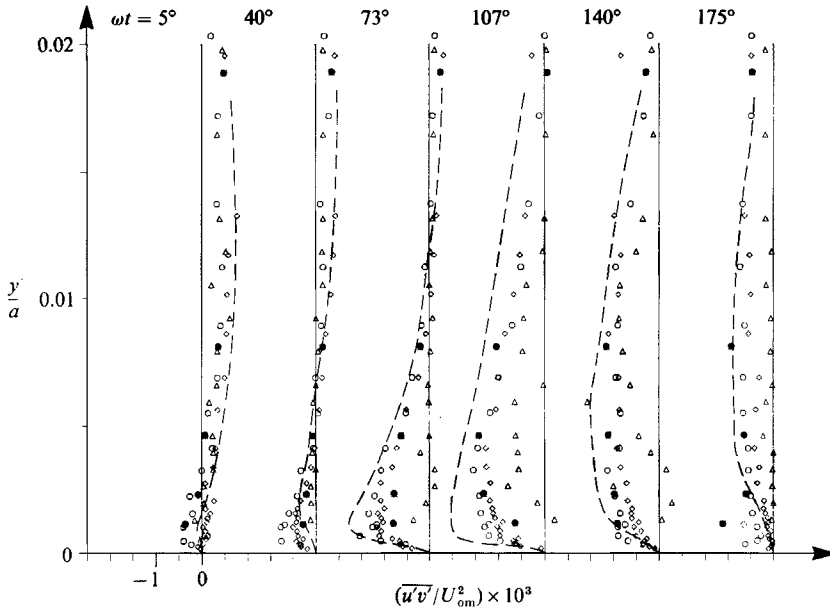
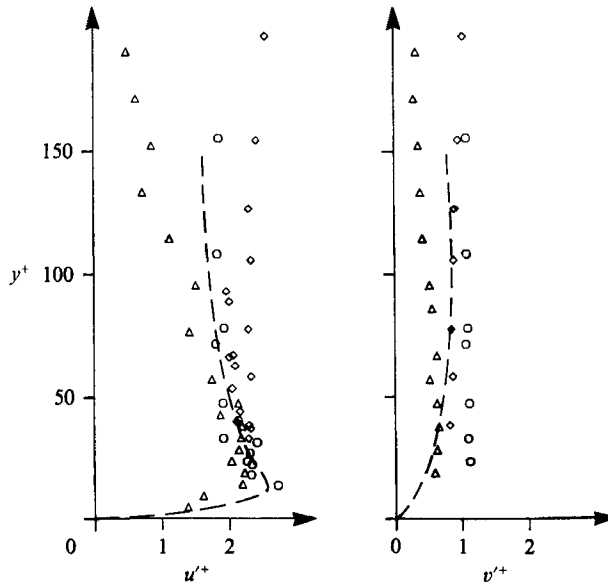FIGURE 21. Reynolds stress for different Re. Smooth bed. Symbols as figure 18.

FIGURE 22. R.m.s. values of u' and v' for different Re. Smooth bed. $\omega t = 107°$.
Symbols as figure 18.

Considering only these fully developed-turbulent-regime Re, it is apparent from figures 19 and 20 that the turbulence level $((\overline{u'^2})^{\frac{1}{2}}/U_{0m}$ and $(\overline{v'^2})^{\frac{1}{2}}/U_{0m})$ decreases, as Re increases. This is in full accord with the early steady boundary-layer flow measurements where similar results were obtained (Laufer 1951).

Figure 22 presents the u' and v' profiles, normalized with the inner-flow parameters, for the same Re as in the previous figures and at $\omega t = 107°$. At this phase value the
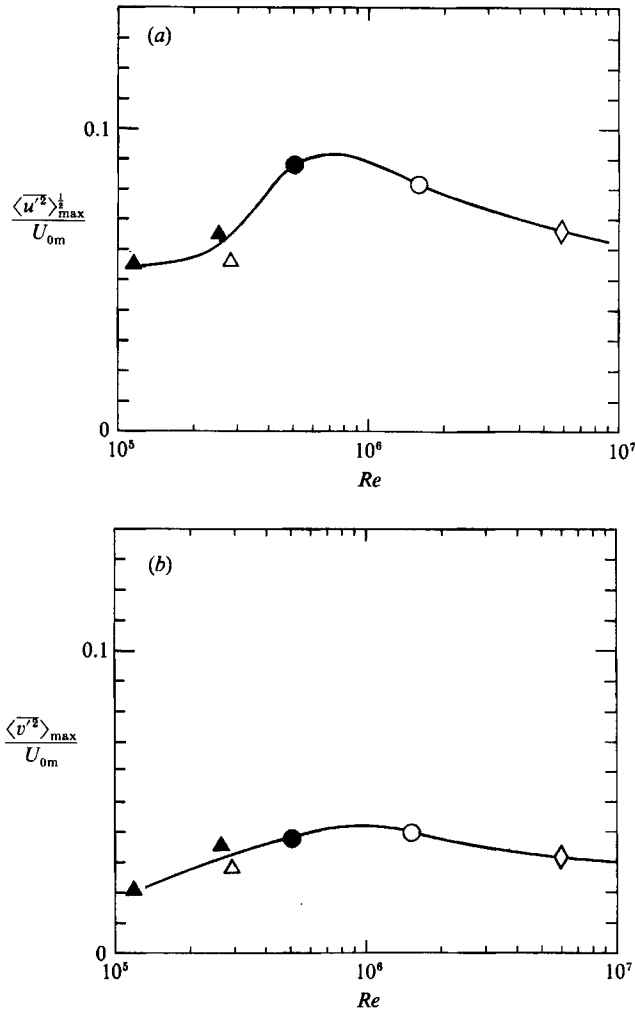
FIGURE 23. Peak values of period-averaged turbulence intensities as function of Re. Smooth bed. ○, ◇, present experiments, Tests 8 and 10; ●, Spalart & Baldwin's (1987) direct Navier–Stokes simulation; △, Hino *et al.* (1983); ▲, Sleath's (1987) 0.2 mm sand-bed tests where $k_s^+ \approx 10$.

flow can be assumed to have reached the fully developed turbulent state (figure 8). As the flow experiences almost zero pressure gradient at this stage of the motion ($\omega t = 107°$), the results shown in figure 22, should be directly comparable to those obtained in zero pressure gradient, steady boundary-layer flows such as in Laufer's (1951) experiments and also in Spalart & Leonard's (1987) and Spalart's (1988) numerical simulations. Figure 22 exhibits exactly the same Re-dependence as the latter works.

Finally, figure 23 presents the peak values of period-averaged turbulence levels as function of Re. Here $\langle \overline{u'^2} \rangle^{\frac{1}{2}}$ is the period-averaged value of r.m.s. u', and $\langle \overline{u'^2} \rangle^{\frac{1}{2}}_{max}$ is the peak value of $\langle \overline{u'^2} \rangle^{\frac{1}{2}}$ in its variation with respect to y. $\langle \overline{v'^2} \rangle^{\frac{1}{2}}_{max}$ is defined in the same way. The turbulence levels appear to be somewhat smaller in the $Re = 2.8 \times 10^5$ and $Re = 2.5 \times 10^5$ tests than those in the others. This behaviour can be attributed to the fact that the flow at this Re experiences the transitional flow regime most of the time during the course of oscillations.
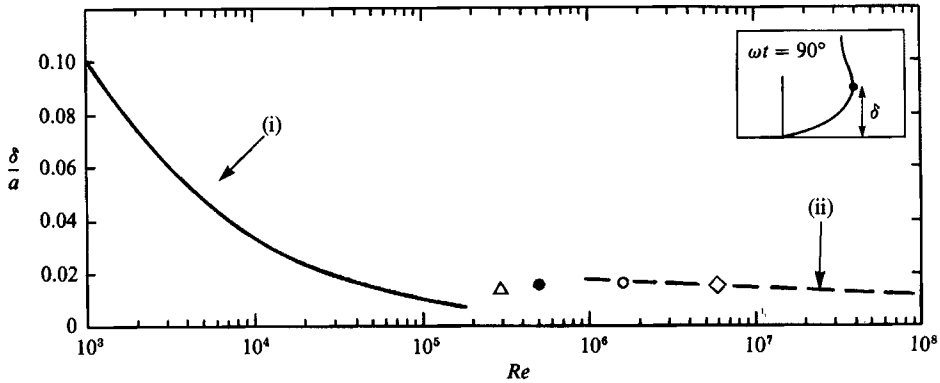
FIGURE 24. Boundary-layer thickness as function of Re. Smooth bed. (i) Laminar, equation (15). (ii) Fredsøe's (1984) theoretical solution; $\diamondsuit$, $\bigcirc$, present experiments, Tests 8 and 10; $\bullet$, Spalart & Baldwin's (1987) direct Navier–Stokes simulation; $\triangle$, Hino *et al.* (1983).

4.4. *Boundary-layer thickness*

Figure 24 presents the non-dimensional boundary-layer thickness δ/a plotted against Re. The definition of δ is indicated in the figure. The laminar-flow relation can readily be obtained from the known laminar boundary-layer solution (Batchelor 1967) and expressed as

$$\frac{\delta}{a} = \frac{3\pi}{4}\left(\frac{2}{Re}\right)^{\frac{1}{2}}. \tag{15}$$

In the figure Hino *et al.*'s (1983) experimental result, Spalart & Baldwin's (1987) direct Navier–Stokes simulation result and Fredsøe's (1984) integration of the momentum equation result are plotted together with the results of the present test. The agreement between the experimental data and the theoretical results is quite good.

5. Rough wall

5.1. *Fully developed turbulent flow*

Figures 25–28 present the rough-bed counterpart of the data depicted in figures 12–14 where $Re = 6 \times 10^6$. Note that the roughness Reynolds number of the tests is $k_s^+ = 84$. Therefore we can safely assume that the bed in these tests behaved as a completely rough wall. Also included in figures 25–28 are the corresponding smooth-bed results, to facilitate comparison. Recall that the free-stream conditions (table 1) are maintained exactly the same in the two experiments. Therefore comparison can be made on the same basis.

From figures 25–28, the following points appear to be noteworthy. (i) The description given in §4.2 of how the flow and turbulence evolve during one half-cycle of the flow is qualitatively the same for the rough-bed flows too. (ii) The introduction of roughness, however, results in a decrease in the mean flow velocity and an increase in the turbulence quantities u', v' and $\overline{u'v'}$. (iii) However, this effect tends to disappear with the distance from the bed: the mean flow velocity is practically the same for the two cases for distances $y/a \gtrsim 0.01$. The same is also true for the turbulence quantities, although this time the effect of roughness disappears at somewhat larger distances from the bed, namely for $y/a \gtrsim 0.03$. The decrease in the mean
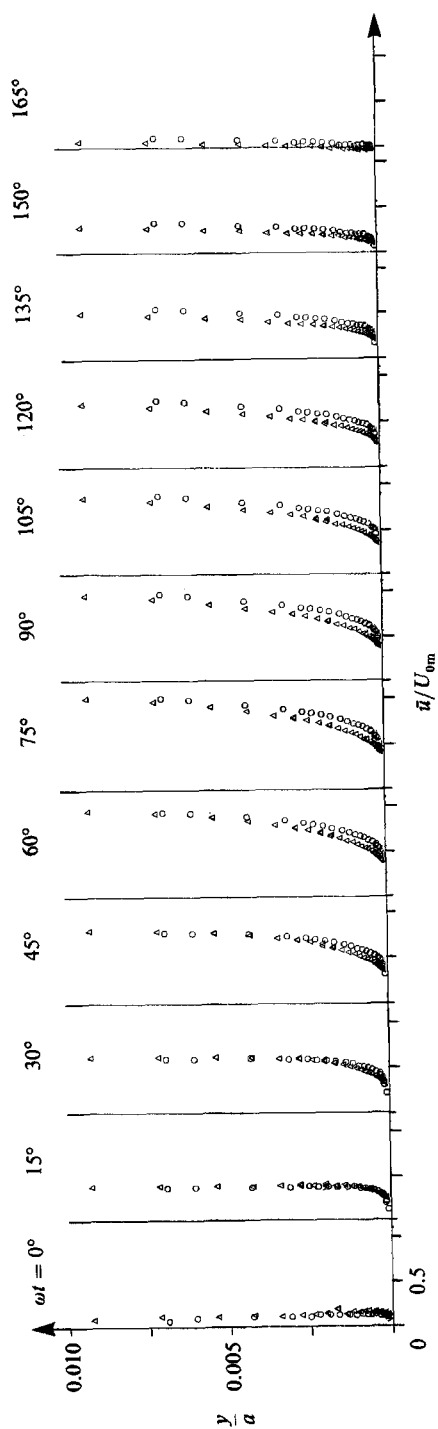
FIGURE 25. Mean velocity distributions. $Re = 6 \times 10^6$. ○, Smooth bed (Test 10); △, rough bed ($a/k_s = 3700$, Test 13).
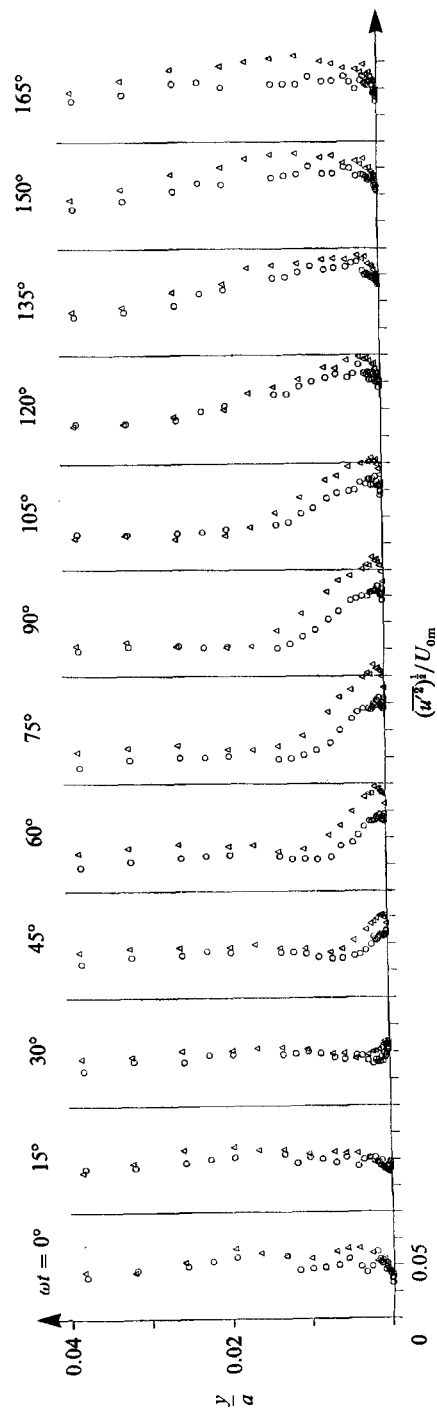

FIGURE 26. R.m.s. value of u'. Symbols and conditions as figure 25.

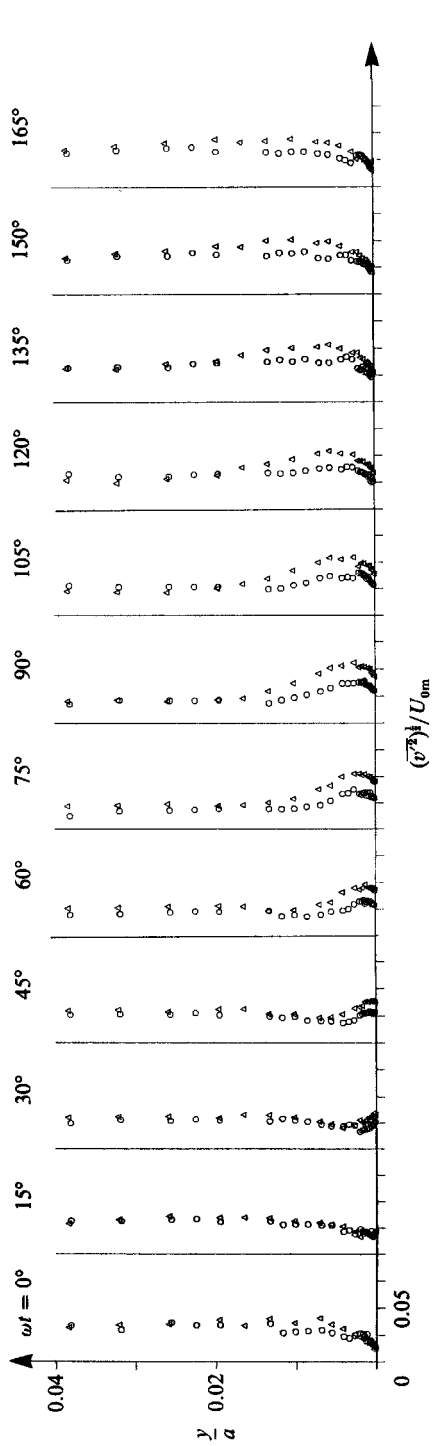FIGURE 27. R.m.s. value of v'. Symbols and conditions as figure 25.
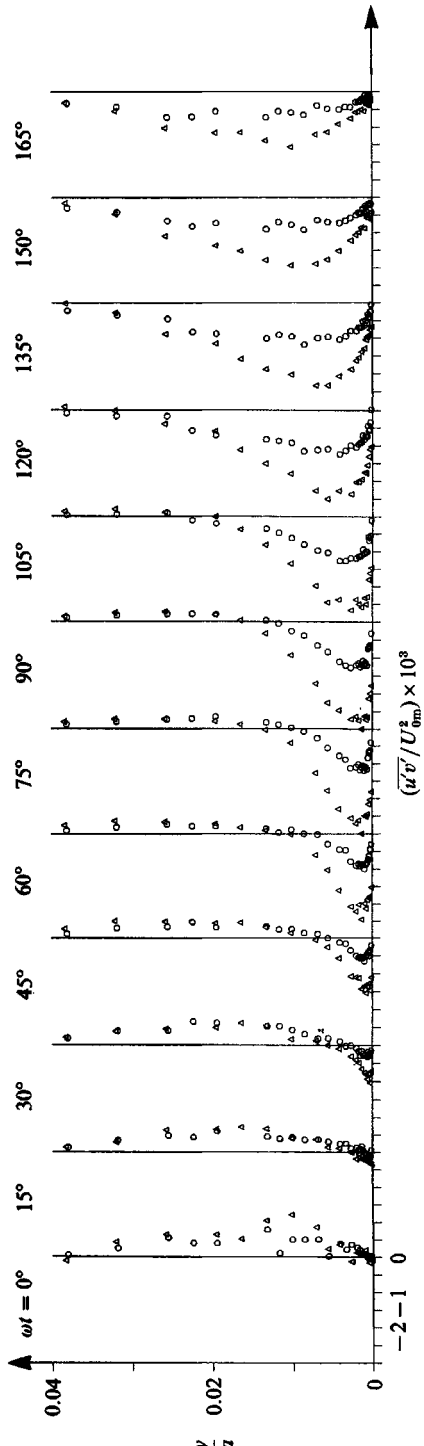
FIGURE 28. Reynolds stress. Symbols and conditions as figure 25.

velocity is due to the retarding effect of the rough boundary while the increase in the turbulence quantities is due to the enhancement of the momentum transfer by the presence of the roughness elements. (iv) It is interesting to note that the flow begins to feel the effect of roughness only after ωt reaches the value of about $15°$. This is because the temporal value of the roughness Reynolds number of the bed, namely $k_s U_f / \nu$, is still far too small for these phases for the bed to act as a completely rough boundary and, as a result, the flow quantities for this short interval of time remain practically unchanged, irrespective of whether the boundary is smooth or rough. It should be noted that this effect is even more pronounced when the results of Test 12 (rough bed with $k_s^+ = 44$) are compared with those of Test 8 (smooth bed) where $Re = 1.6 \times 10^6$. (The data are not given here for reasons of space; but see Jensen 1989.) Indeed, the flow in this latter case begins to feel the effect of roughness at an even later stage, namely $\omega t \approx 45°$.

5.2. *Effect of* a/k_s

In fully developed turbulent flows over a completely rough boundary, the quantities are dependent upon one single parameter, namely a/k_s. Figure 29 presents the mean velocity profiles at various phase values for three different values of a/k_s (124, 730 and 3700), while figures 30 and 31 present r.m.s. u' and r.m.s. v' distributions for two different values of a/k_s (138, 3700). It is important to note that the Reynolds numbers and the values of a/k_s of the tests depicted in these figures are such that the flows are in the fully developed turbulent regime where the Reynolds-number dependence disappears, and consequently a/k_s becomes the only parameter responsible for the variation of turbulence quantities (see Sleath 1988).

One of the three tests presented in figure 29, that corresponding to $a/k_s = 124$ profiles, comes from Jonsson & Carlsen (1976). Likewise, the test corresponding to $a/k_s = 138$ in figures 30 and 31 comes from Sleath (1987). (Note that in Sleath's work the k_s value was not obtained through the log fit procedure but simply was set to $2d$, where d is the grain size). The reason why the profiles corresponding to these two studies are not presented in the same figure is that Jonsson's study does not include turbulence measurements, while Sleath's work does not give the mean velocity data in the form which can be adopted for the present purpose.

As far as the mean-velocity plot is concerned (figure 29), it is seen that the logarithmic layer is established very early in the acceleration stage in all the three cases depicted. However, the difference between these three cases is that the thickness of the logarithmic layer is the largest in the $a/k_s = 3700$ case, and it gets smaller as the value of a/k_s decreases. This behaviour can be explained by reference to figure 34 which illustrates the variation of the boundary-layer thickness δ/k_s: the larger the value of a/k_s, the larger the boundary-layer thickness δ/k_s, and the larger the boundary-layer thickness, the larger the thickness of the logarithmic layer. Thus the thickness of the logarithmic layer should be larger for larger a/k_s values.

Concerning the variation of the turbulence quantities with respect to a/k_s, figures 30 and 31 give a fairly consistent picture about the role that a/k_s plays as the governing parameter. The figures indicate that the smaller the value of a/k_s (or the larger the roughness k_s/a), the larger the turbulence level. This can be linked with the fact that the momentum transfer is greatly enhanced with increase in the size of roughness elements.

Figure 32 presents the period-averaged turbulence data, namely $\langle \overline{u'^2} \rangle^{\frac{1}{2}}_{max}$ and $\langle \overline{v'^2} \rangle^{\frac{1}{2}}_{max}$, where the large-$a/k_s$ test results are plotted on the diagrams given by Sleath (1987, 1988). Sleath pointed out that his results tend to a unique curve at high Re.
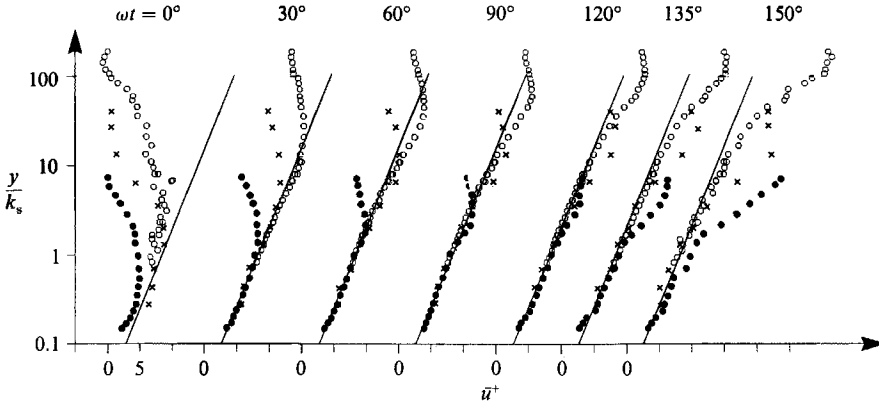
FIGURE 29. Mean velocity distributions in semi-log plot for different a/k_s values. Rough bed. ●, $a/k_s = 124$, Jonsson & Carlsen (1976); ×, $a/k_s = 730$, Test 15; ○, $a/k_s = 3700$, Test 13.
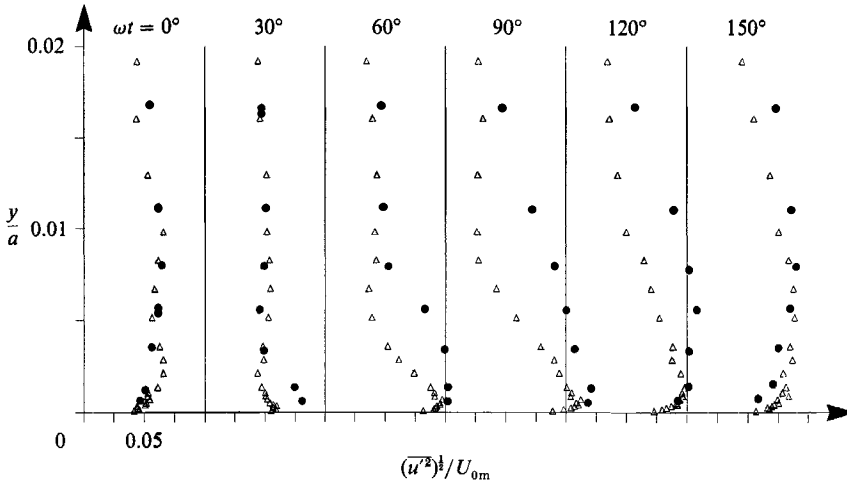

FIGURE 30. R.m.s. value of u' for different a/k_s values. Rough bed. ●, $a/k_s = 138$, Sleath (1987); △, $a/k_s = 3700$, Test 13.
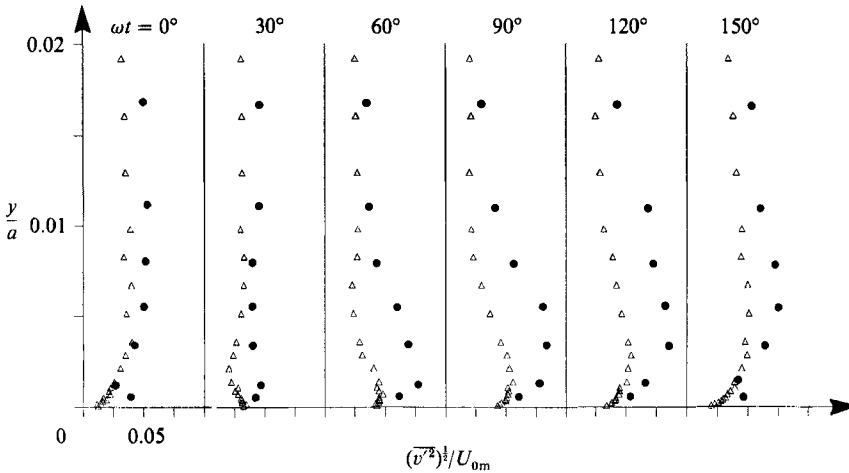

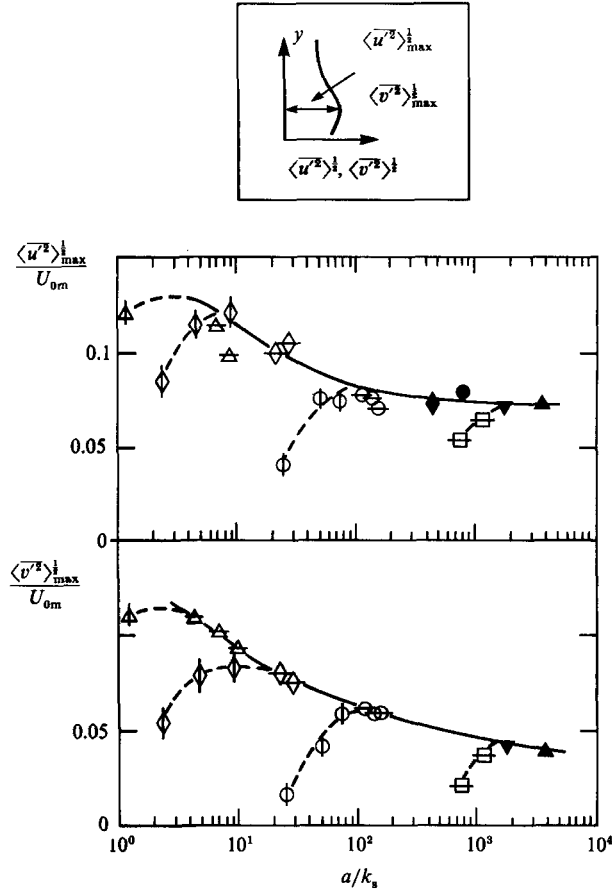FIGURE 31. R.m.s. value of v' for different a/k_s values. Symbols and conditions as figure 31.

FIGURE 32. Peak values of period-averaged turbulence intensities as function of a/k_s. Rough bed. Sleath (1987, 1988): $\triangle$, $10^5 < Re < 5 \times 10^5$, $k_s^+ \approx 5000$; $\triangle$, $10^4 < Re < 10^5$, $k_s^+ = 4000$; $\ominus$, $10^5 < Re < 5 \times 10^5$, $k_s^+ \approx 950$; $\diamondsuit$, $10^3 < Re < 10^5$, $390 \leqslant k_s^+ \leqslant 500$; $\ominus$, $10^5 < Re < 5 \times 10^5$, $130 \leqslant k_s^+ \leqslant 170$; ϕ, $10^3 < Re < 10^5$, $40 \leqslant k_s^+ \leqslant 100$; $\boxminus$, $Re = 10^5$, $k_s^+ = 8$ and $Re = 2.5 \times 10^5$, $k_s^+ = 11$. Present experiments: $\blacklozenge$, $Re = 9 \times 10^5$, $k_s^+ = 142$, Test 14; $\bullet$, $Re = 5.2 \times 10^6$, $k_s^+ = 490$, Test 15; $\blacktriangledown$, $Re = 1.6 \times 10^6$, $k_s^+ = 44$, Test 12; $\blacktriangle$, $Re = 6 \times 10^6$, $k_s^+ = 88$, Test 13.

It is remarkable that the present high-Re experiments confirm Sleath's observation, as they, together with Sleath's results, appear to collapse onto one common curve (the solid lines). It should be noted, however, that the curves originally suggested by Sleath appear to be somewhat below the present ones at large a/k_s values. This is because Sleath's curves at large a/k_s are mainly based on his 0.2 mm sand test results and the bed in these tests does not behave as a completely rough boundary, as mentioned previously.

Figure 32 shows that the period-averaged turbulence level decreases with increasing a/k_s, yet this decrease occurs at a slower rate for larger values of a/k_s. Furthermore, the figure indicates that $\langle \overline{u'^2} \rangle^{\frac{1}{2}}_{\max}/U_{0m}$ tends to a constant value of about 0.07 and $\langle \overline{v'^2} \rangle^{\frac{1}{2}}_{\max}/U_{0m}$ to about 0.04, as a/k_s tends to very large values.

5.3. *Velocity-defect law*

Figure 33 presents the time evolution of the velocity distributions in the velocity-defect-law form, $\bar{u} - U_0 = U_{fm} f(y/\hat{\delta}, \omega t)$, where the results for the rough-bed tests are
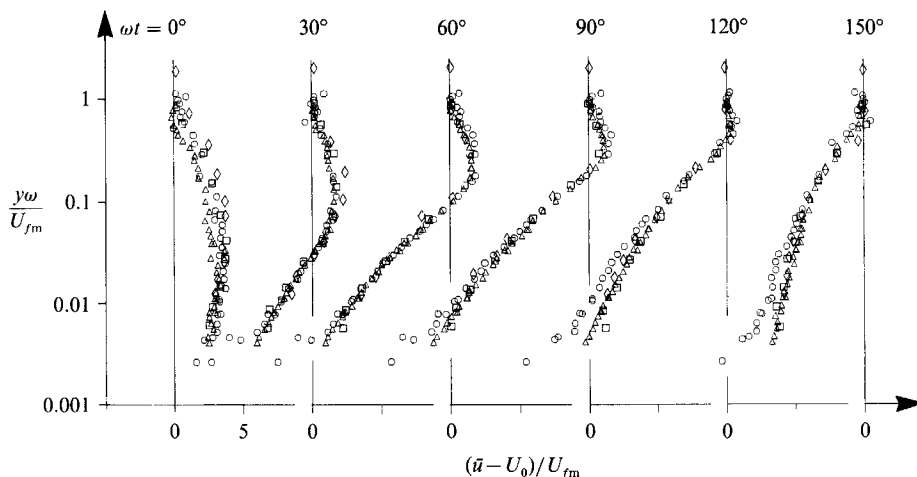
FIGURE 33. Velocity-defect law. ◯, Test 10; ◇, Test 14; △, Test 13; ☐, Test 15.
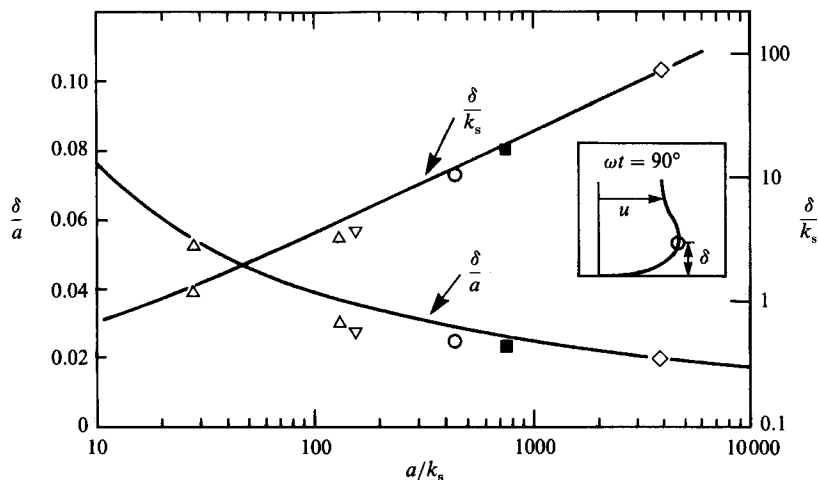
FIGURE 34. Boundary-layer thickness. Rough bed. ◇, ◯, ■, present tests 13, 14 and 15, respectively; △, Jonsson & Carlsen (1967); ▽, Sleath (1987). Solid curve, Fredsøe's (1984) theoretical solution.

plotted together with those for the smooth bed. Here $\hat{\delta} = U_{fm}/\omega$, a characteristic lengthscale representative for the boundary-layer thickness. From diffusion considerations, the boundary-layer thickness δ can be written as $\delta \sim (\nu_T t)^{\frac{1}{2}}$ where $t = \frac{1}{4}T$ (corresponding to $\omega t = 90°$, see figure 24) and ν_T, the cross-sectional average turbulent diffusion coefficient, $\nu_T \sim \delta U_{fm}$. This leads to $\delta \sim U_{fm}/\omega$, which indicates that $\hat{\delta} = U_{fm}/\omega$ is indeed a characteristic lengthscale representative for the boundary-layer thickness. In figure 33 the actual boundary-layer thickness is abandoned in favour of $\hat{\delta}$, simply to avoid the uncertainties involved in the experimental determination of the actual boundary-layer thickness.

Figure 33 shows remarkably that the velocity distributions obtained for a variety of a/k_s and Re values fall on common curves when plotted in this form except at locations near the wall where the wall influence is inevitable.

5.4. *Boundary-layer thickness*

Figure 34 gives the boundary-layer thickness plotted against a/k_s. In the figure the solid curve represents Fredsøe's (1984) theoretical solution obtained through the integration of the momentum equation. The agreement between the experiments and Fredsøe's theoretical result is quite good.

6. Conclusions

The main results of the present study regarding the smooth-bed oscillatory boundary layers are summarized as in the following.

(i) The present experiments indicate that the transitional flow regime occurs over quite a wide range of Re. The transition to turbulence first occurs at $Re \approx 10^5$, as has been recognized previously. This takes place at phases just prior to the near-bed flow reversal. As the flow Re is increased, however, more and more portions of the flow half-cycle join the fully developed turbulent motion, yet the present experiments indicate that, even at Re as large as 1.6×10^6, there is still some portion of the half-cycle (namely $\omega t \lesssim 45°$) where the flow regime is not a fully developed turbulent one.

(ii) The familiar logarithmic layer is present in a turbulent smooth-wall oscillatory boundary layer. It comes into existence some time after the flow reverses, and grows in size as the flow progresses. The larger the Reynolds number, the earlier the logarithmic layer is established.

(iii) The turbulence in the boundary layer evolves steadily throughout one half-cycle of the motion. The wall-generated turbulence has become spread across the depth by the time that the flow reversal occurs.

(iv) The distributions of the fully developed-regime turbulence quantities, when normalized with the inner-flow parameters, appear to be in reasonable accord with the corresponding steady boundary-layer distributions throughout the half-cycle of the flow, except at the early stages of the acceleration phase and at the late stages of the deceleration phase of the motion.

(v) As far as the effect of Re is concerned, the turbulence quantities, when normalized with the outer-flow parameters, appear to change weakly with Re at locations away from the bed. Near the bed, however, there is a marked Re-dependence. The manner in which the quantities change with respect to Re is exactly the same as in steady boundary-layer flows.

(vi) It seems that a tracker-based LDA system is unable to measure the Reynolds stresses very close to a smooth wall, owing to the disturbing effect of reflected laser light from the wall surface.

The main results of the present study regarding the rough-bed oscillatory boundary layers, on the other hand, are summarized as follows.

(i) The introduction of roughness on the bed, even as small as $k_s/a = 2.7 \times 10^{-4}$ ($a/k_s = 3700$), at $Re = 6 \times 10^6$, leads to marked differences in the response of the boundary layer. The turbulent intensities are increased by 50 % and the Reynolds stresses by as much as 100 %.

(ii) The effect (i) tends to disappear, however, with the distance from the bed. For y/a-values larger than about 0.03, practically no difference has been measured between the smooth bed and the rough bed.

(iii) The logarithmic layer exists also in the rough-wall oscillatory boundary-layer flows. The way in which it forms and develops is similar to that in smooth-bed oscillatory boundary-layer flows.

(iv) The fully developed-regime turbulence quantities are dependent on the roughness parameter a/k_s. This dependence practically disappears at locations away from the bed, but is felt strongly near the bed.

REFERENCES

BAKKER, W. T. 1974 Sand concentration in an oscillatory flow. *Proc. 14th Conf. Coastal Eng.*, Copenhagen, pp. 1129–1148.

BATCHELOR, G. K. 1967 *An Introduction to Fluid Dynamics*. Cambridge University Press.

COLES, D. 1956 The Law of the wake in a turbulent boundary layer. *J. Fluid Mech.* **1**, 191–226.

DRIEST, E. R. VAN 1956 On turbulent flow near a wall. *J. Aero. Sci.* **23**, 1007–1011.

FREDSØE, J. 1984 Turbulent boundary layer in wave-current motion. *J. Hyd. Engng ASCE* **110**, 1103–1120.

HAGATUN, K. & EIDSVIK, K. J. 1986 Oscillating turbulent boundary layers with suspended sediment. *J. Geophys. Res.* **91** (C11), 13045–13055.

HANRATTY, T. J. & CAMPBELL, J. A. 1983 Measurements of wall shear stress. In *Fluid Mechanics Measurements* (ed. R. J. Goldstein). Hemisphere.

HINO, M., KASHIWAYANAGI, M., NAKAYAMA, A. & HARA, T. 1983 Experiments on the turbulence statistics and the structure of a reciprocating oscillatory flow. *J. Fluid Mech.* **131**, 363–400.

HINO, M., SAWAMOTO, M. & TAKASU, S. 1976 Experiments on transition to turbulence in an oscillatory pipe flow. *J. Fluid Mech.* **75**, 193–207.

JENSEN, B. L. 1989 Experimental investigation of turbulent oscillatory boundary layers. Thesis, Technical University of Denmark, Institute of Hydrodynamics and Hydraulic Engineering, Lyngby, Denmark, in partial fulfillment of the requirements for the degree of Licentiata Technices.

JONSSON, I. G. 1963 Measurements in the turbulent wave boundary layer. *Proc. 10th Congr. IAHR*, London, Vol. 1, pp. 85–92.

JONSSON, I. G. & CARLSEN, N. A. 1976 Experimental and theoretical investigations in an oscillatory turbulent boundary layer. *J. Hydraul. Res.* **14**, 45–60.

JUSTESEN, P. 1988a Turbulent wave boundary layers. *Series Paper* 43. Thesis, The Technical University, University of Denmark, Institute of Hydrodynamics and Hydraulic Engineering, Lyngby, Denmark, in partial fulfillment of the requirements for the degree of Licentiata Technices.

JUSTESEN, P. 1988b Prediction of turbulent oscillatory flow over rough beds. *Coastal Engng* **12**, 257–284.

JUSTESEN, P. & FREDSØE, J. 1985 Distribution of turbulence and suspended sediment in the wave boundary layer. *Prog. Rep.* 62, pp. 61–67. Inst. of Hydrodyn. & Hyd. Engrg., Technical Univ. Denmark.

KAJIURA, K. 1968 A model for the bottom boundary layer in water waves. *Bull. Earthquake Res. Inst.* **45**, 75–123.

KAMPHUIS, J. W. 1975 Friction factor under oscillatory waves. *J. Waterways, Port Coastal Engng Div. ASCE* **101** (WW2), 135–144.

LAUFER, J. 1951 Investigation of turbulent flow in a two-dimensional channel. *NACA Rep.* 1053.

LUNDGREN, H. & SØRENSEN, T. 1958 A pulsating water tunnel. *Proc. 6th Intl Conf. on Coastal Engineering*, Miami, Fl., pp. 356–358. Council on Wave Research, The Engng Foundation, Engineering Field Station, University of California, Richmond, CA.

SLEATH, J. F. A. 1984 *Sea Bed Mechanics*. Wiley.

SLEATH J. F. A. 1987 Turbulent oscillatory flow over rough beds. *J. Fluid Mech.* **182**, 369–409.

SLEATH, J. F. A. 1988 Transition in oscillatory flow over rough beds. *J. Waterway, Port, Coastal Ocean Engng Div. ASCE*, **114**, 18–33.

SPALART, P. R. 1988 Direct simulation of a turbulent boundary layer. *J. Fluid Mech.* **187**, 61–98.

SPALART, P. R. & BALDWIN, B. S. 1987 Direct simulation of a turbulent oscillating boundary layer. NASA *Tech. Mem.* 89460, Ames Research Center, Moffett Field, Ca. (Also in *Turbulent Shear Flows 6*, Springer, in press.)

SPALART, P. R. & LEONARD, A. 1987 Direct numerical simulation of equilibrium turbulent boundary layers. In *Turbulent Shear Flows 5* (ed. F. Durst, B. E. Launder, J. L. Lumley, F. W. Schmidt & J. H. Whitelaw), pp. 234–252. Springer.

SUMER, B. M., JENSEN, B. L. & FREDSØE, J. 1987 Turbulence in oscillatory boundary layers. In *Advances in Turbulence* (ed. Gt. Comte-Bellot & J. Mathieu), pp. 556–567. Springer.